ION CHEMISTRY OF HYDROGENATED PAHs

Malick DIEDHIOU

Thesis submitted to the
in partial fulfillment of the requirements for
the Master's degree in Chemistry

April 20, 2020

Candidate	Supervisor
Malick Diédhiou	Dr. Paul M Mayer

Abstract

Polycyclic aromatic hydrocarbons (PAHs) are a class of organic molecules suggested to constitute roughly 20% of carbon in the interstellar medium (ISM). These species exist in both neutral and ionic forms and both are potentially involved in processes such as H_2 formation. Catalyzing H_2 formation necessarily involves the participation of hydrogenated PAHs as reaction intermediates. Employing tandem mass spectrometry and imaging photoelectron photoion coincidence spectroscopy and theory, we have explored the unimolecular reactions of five ionized hydrogenated PAHs that vary in degree and position of hydrogenation: tetralin (1,2,3,4-tetrahydronaphthalene), 9,10-dihydroanthracene ($DHA^{+\bullet}$), 1,2,3,4-tetra- and 1,2,3,4,9,10-hexa-hydrophenanthrene ($THP^{+\bullet}$ and $HHP^{+\bullet}$) and 1,2,3,4,5,6,7,8-octahydroanthracene ($OHA^{+\bullet}$). The major reactions observed were the losses of the hydrocarbons $CH_3^\bullet$, C_2H_4 and $C_3H_5^\bullet$ together with $H^\bullet$ atom loss. RRKM modeling of the iPEPICO data suggested that the unimolecular chemistries were based around a two-well potential energy surface in each case. Ionized tetralin can lose all four neutrals via H-shift and ring-opening reactions, or $CH_3^\bullet$ and C_2H_4 after interconversion to the 1-methylindane ion, a process similar to that found for ionized 1,2-dihydronaphthalene (isomerizing to form the 1-methylindene ion structure). $DHA^{+\bullet}$ exhibits the same reactions previously observed for 1,2-dihydronaphthalene and 9,10-dihydrophenanthrene, namely competing loss of $H^\bullet$ and $CH_3^\bullet$. However, the energy required for $H^\bullet$-loss, as predicted by RRKM modeling of the iPEPICO results, was lower than the latter ions, presumably due to an expansion of the electron delocalization across the central ring upon dehydrogenation. $OHA^{+\bullet}$ behaves similarly to ionized tetralin, displaying losses of $H^\bullet$, $CH_3^\bullet$, C_2H_4 and $C_3H_5^\bullet$ in its collision induced dissociation (CID) mass spectra, but under iPEPICO conditions $CH_3^\bullet$-loss is not observed. $THP^{+\bullet}$ and

HHP$^{+\bullet}$ have aspects of both DHA$^{+\bullet}$ and OHA$^{+\bullet}$ chemistries, displaying losses of H$^{\bullet}$, CH$_3^{\bullet}$, C$_2$H$_4$ and C$_3$H$_5^{\bullet}$. Minimum energies for all observed reaction channels were thus obtained, together with selected mechanisms computationally explored at the B3-LYP/6-31+G(d,p) level of theory. The trend in reactivity in going from tetralin and DHA$^{+\bullet}$ to THP$^{+\bullet}$, HHP$^{+\bullet}$ and ultimately OHA$^{+\bullet}$ sees decreasing abundance of H$^{\bullet}$ and CH$_3^{\bullet}$-loss and an increasing dominance of the formation of C$_2$H$_4$, C$_3$H$_5^{\bullet}$ and higher hydrocarbons with degree of hydrogenation as isomerization to a methyl-substituted ion becomes less significant. As this isomerization decreases in significance, the ions become sources of small hydrocarbon molecules and not hydrogen atoms or molecules.

Acknowledgments

Firstly, I would like to thank Allah for all, to thank my family (my parents and to my brothers and sisters) for supporting me spiritually throughout this thesis and my life in general.

I would like to express my sincere gratitude to my supervisor, Dr. Paul Mayer, for giving me the opportunity to continue my study in this high-level University, for the continuous support, for his patience, motivation, and immense knowledge. He was always available for discussion and never stopped for giving excellent advice and feedback and his guidance helped me in all the time of research and writing of this thesis. I could not have imagined having a better advisor

A big thank to the rest of my thesis committee: Dr. Javier Giorgi and Dr. David Bryce, for accepting to examine my thesis.

My sincere thanks also goes to Dr. Brandi West for her support, she was also my mentor, to Dr. Sander Mommers and Dr. Sharon Curtis for their knowledge about the instrument. Without their precious support it would not be possible to conduct this research.

I thank my fellow lab-mates: Sean Overton, Nick Zinck, Bethany Lowe and Norah Alotaibi for all their support, encouragement andthe stimulating discussions, and for all the fun we have had in the lab.

Table of Contents

List of Figures

List of Tables

List of Abbreviations

APCI	Atmospheric Pressure Chemical Ionization
B3-LYP	Becke 3-Parameter (Exchange), Lee, Yang and Parr
CID	Collision induced dissociation
DFT	Density functional theory
DIBs	Diffuse interstellar bands
(E)	Reactant ion density of states
E_0	Activation energy at 0 K (eV)
E_{com}	Center of mass collision energy
E_{lab}	Lab frame collision energy
iPEPICO	imaging photoelectron photoion coincidence spectroscopy
IR	Infrared
ISM	Interstellar medium
IVR	Intramolecular vibrational relaxation
MAH	Monocyclic aromatic hydrocarbon
MCP	Microchannel plate
MS	Mass spectrometry
MS/MS	Tandem mass spectrometry
m/z	Mass-to-charge ratio
$N^‡$	Transition state sum of state

PAHs	Polycyclic aromatic hydrocarbons
RF	Radio frequency
RRKM	Rice–Ramsperger–Kassel–Marcus
SLS	Swiss Light Source
T_{eff}	Effective temperature
Ti	Initial temperature
TOF	Time of flight
$TS^{‡}$	Transition state
UV	Ultraviolet
ZPE	Zero Point Energy
α	alpha (Kev^{-1})
$\Delta^{‡}S$	Entropy of activation

Chapter 1: Introduction

This section gives a brief overview of the connection between polycyclic aromatic hydrocarbons and the interstellar medium. We describe the physical conditions in dense clouds and the processes believed to be involved in star formation that can be attributed to interstellar chemistry.

1.1. The molecules in the interstellar medium

The interstellar medium (ISM) is the region in space between the stars and is composed of H and He gases, as well as dust. It ranges from incredibly hot (10,000 K) and diffuse (1 atom cm^{-3}) regions, to cold (10 K) and dense (>10^4 atoms/molecules cm^{-3}) clouds. Gases make up the main part of the mass of the ISM. The residue is a mix of grains produced in dying stars and modified in the ISM. Although the residue includes just a small quantity of material in the ISM by mass (i.e., 1%), it plays a fundamentally important role in interstellar chemistry. While gas is generally transparent to photons from the near ultraviolet to the far-infrared, dust absorbs and scatters this same energy. This procedure is alluded to as "extinction." Residue would then be able to fill in as a "shield" from ultraviolet energy in denser regions so that more complex reactions might occur in the surrounding gas and on the grains themselves in surface mediated reactions.[1]

Many of the molecules found in meteoritic extracts can be explained through interstellar chemistry. Organic compounds identified in carbonaceous C1 and C2 chondrites include amines and amides; alcohols, aldehydes, and ketones; aliphatic and aromatic hydrocarbons; sulfonic and phosphonic acids; amino, hydroxycarboxylic, and carboxylic acids; purines and pyrimidines; and kerogen-type material.[2,3] These molecules show specific enrichments in D, ^{13}C, and ^{15}N, indicative of their retention of an interstellar heritage. Some of these simple organics may be of true interstellar origin, whereas the more complex molecules may have had simpler interstellar precursors that subsequently reacted in the solar nebula or on a meteorite parent body. The initial interstellar inventory determined which reaction pathways would be most likely for secondary processing in the protosolar nebula, for example, as the result of aqueous alteration on meteoritic parent bodies.[1]

Polycyclic aromatic hydrocarbons (PAHs) are ubiquitous in the ISM, and are additionally prevalent in meteorites.[4,5] Most meteoritic carbon is in form of a kerogen-like material and this might be related with interstellar PAHs.[6] This latter material found in meteorites could have begun in the cool envelopes of carbon stars, although other arrangement sites are possible, for example, in diffuse interstellar gas or by energetic processing of specific ices in dense clouds, or by interaction of CO, N_2, and H_2 on grain surfaces in the solar nebula.[7,8] Since D is consumed in stellar burning, the deuteration of astronomical PAHs can happen in the interstellar medium, specifically in the cold environment of dense molecular clouds. In their developmental cycle, PAH particles solidify out onto grains in dense clouds, where they can get fractionated through energetically driven reactions with deuterated water ice. Also, several ion-molecule gas phase processes will deuterate PAHs.[9]

1.2. Polycyclic aromatic hydrocarbons (PAHs)

Polycyclic aromatic hydrocarbons (PAHs) are a class of organic molecules suggested to constitute roughly 20% of carbon in the interstellar medium (ISM).[10] These species exist in both neutral and ionic forms and both are potentially involved in processes such as H_2 formation and the shielding of organic chemical reactions from high energy radiation.[11] Some example of PAHs molecules are shown in **Figure 1.**

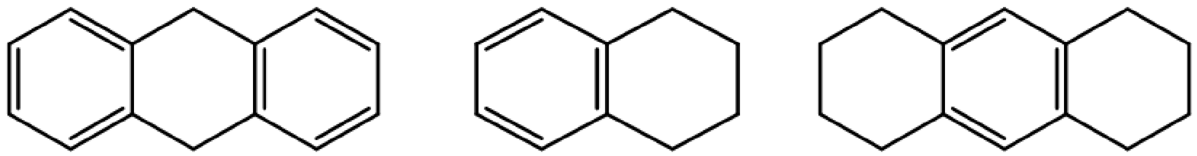

9,10-Dihydroanthracene (DHA)

1,2,3,4-Tetrahydronaphthalene (Tetralin)

1,2,3,4,5,6,7,8-Octahydroanthracene (OHA)

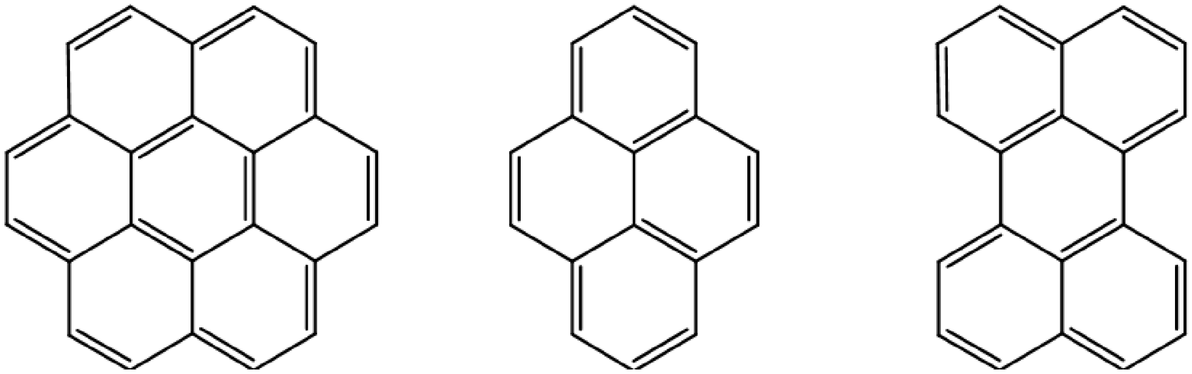

Coronene

Pyrene

Perylene

Figure 1. Examples of PAH molecules.

PAHs in the ISM can absorb UV light from stars, initiating photodissociation to form important interstellar molecules. PAHs can also emit infrared (IR) radiation from electronic excited states leading to vibrationally-excited levels in the ground state.[12] **Figure 2** show some important features that exhibit at 3.3, 6.2, 7.7, 8.6, 11.2 and 12.7 µm in the interstellar IR emission spectrum.[13]

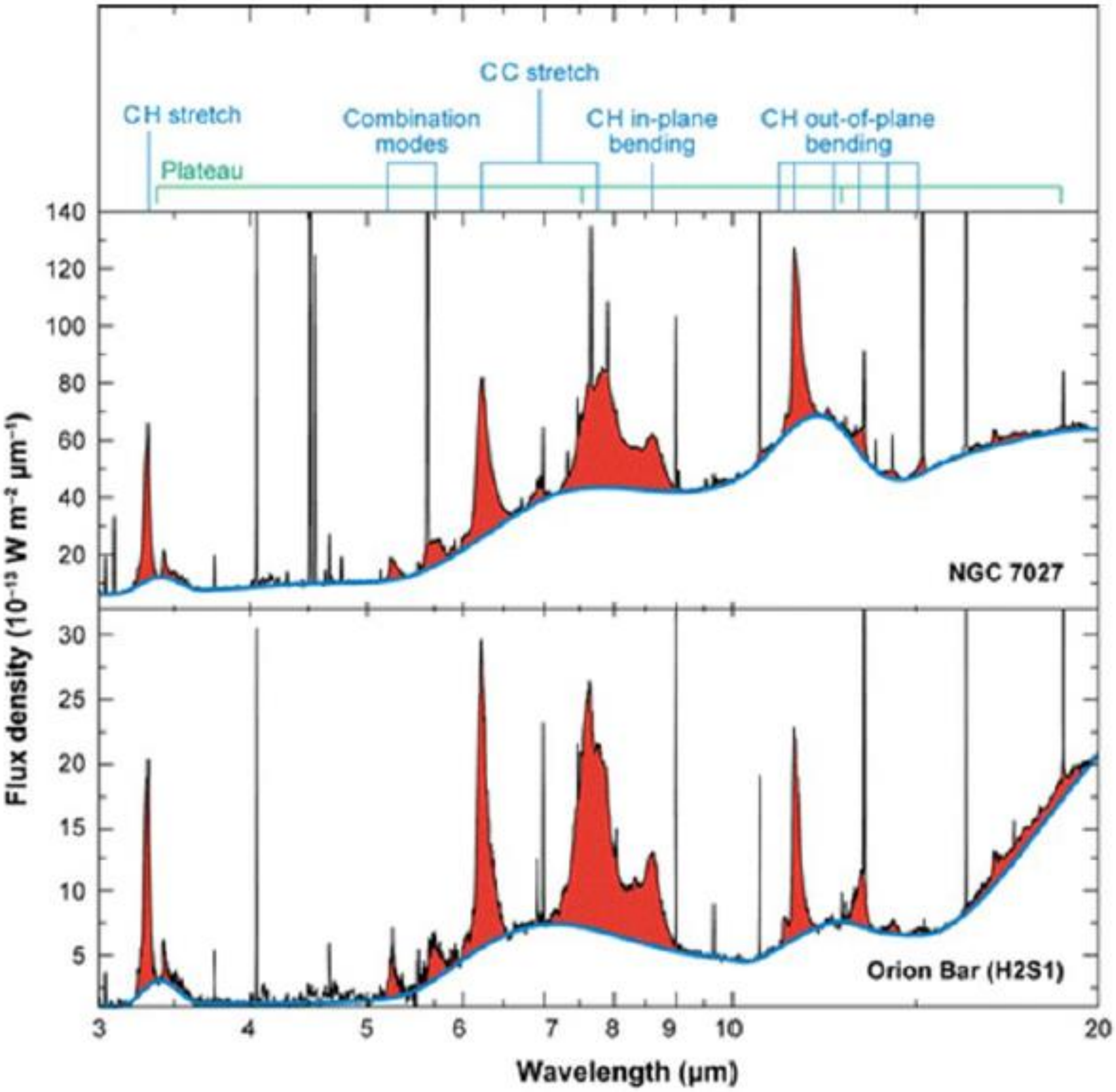

Figure 2. Some of the IR emission spectrum in the interstellar medium showing three spectra selected from the SINGS sample of nuclei of nearby galaxies. These mid-infrared spectra of the photodissociation region in the Orion Bar (H2S1) and in the planetary nebulae NGC 7027 are dominated by a rich set of emission features, which are labeled with the vibrational modes of polycyclic aromatic hydrocarbon molecules at the top. [13]

In addition, broad emission features have been discovered in the 1970's (**Figure 3**). Since the strong band at 6.85 μm was not detected, the peak identified at 11.3 μm (band with carbonates) was refuted, and these observations revealed that the 3.3 and 11.3 μm bands were part of a set of strong bands, collectively with bands at 6.2, 7.7, and 8.6 μm.[14,15]

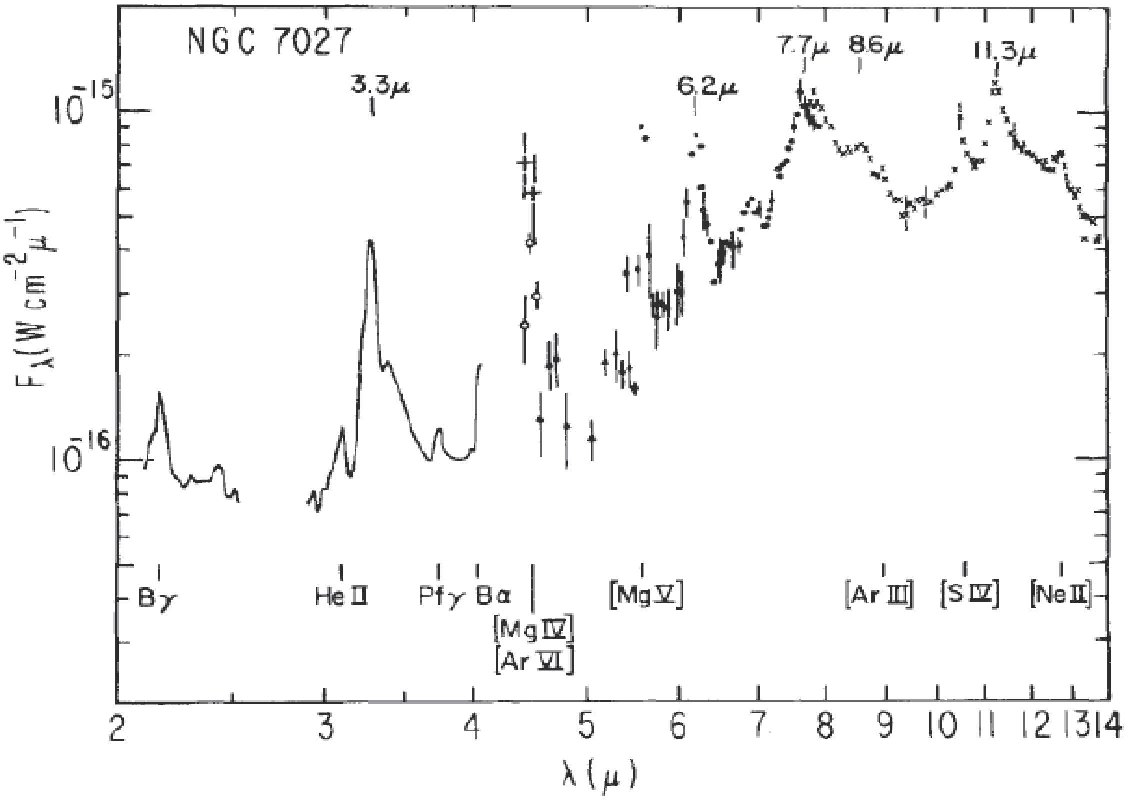

Figure 3. The first overview spectrum of the PAH emission bands.[15] Used with permission from Springer Nature: Astrophys. Space Sci., Unidentified infrared spectral features; S. P. Willner, R. C. Puetter, R. W. Russell, B. T. Soifer; 1979.

Molecular H_2 is the most prolific molecular species found in the interstellar medium (ISM). Whereas it has been long recognized that H_2 is formed on dust grains,[16] investigation of the involved mechanisms is still a very active subject of research.[17,18] One popular theory is that polycyclic aromatic hydrocarbons (PAH) may play a role in the formation of H_2 by acting as catalysts.[10] Atomic hydrogen would adsorb onto the surface of the molecules, thus hydrogenating the PAHs, prior to desorption of H_2.[19-24] This reaction demonstrates the importance of investigating the energetics of not only PAHs but modified PAHs as well, such as hydrogenated species.

There has been very little work done on hydrogenated PAHs and their ions. A theoretical study was conducted on protonated naphthalene which had the $H^\bullet$ loss at an activation energy of 2.71 eV, in good agreement with that for $H^\bullet$ loss from dihydronaphthalene.[25] Reitsma et al. have also shown the effect of hydrogenation on coronene using soft x-ray spectroscopy; they showed that hydrogenation under these high energy conditions acts as a protector for the carbon backbone.[26] The opposite was observed for ionized hydrogenated pyrene studied at high energy collision-induced dissociation (CID) mass spectrometry and action spectroscopy. Here, it was observed that the appearance energy for $CH_3^\bullet$-loss decreased with increasing hydrogenation.[27-29] Hydrogenation of coronene has been explored.[30-32] We previously studied 1,2-dihydronapthalene and 9,10-dihydrophenanthrene by the imaging photoelectron photoion coincidence (iPEPICO) technique.[33] Unlike PAH ions, which display unimolecular losses of $H^\bullet$ (both directly and sequentially) and acetylene, the two dihydroPAH ions undergo reactions leading to loss of $H^\bullet$ and $CH_3^\bullet$. Both were found to isomerize to a methylindene analogue at low internal energies, allowing for $H^\bullet$ and $CH_3^\bullet$-loss, but as internal energy increases this channel was outcompeted by direct $H^\bullet$-loss from the molecular ion. No H_2 was formed in the decomposition of these ions.

1.3. Objectives

The motivation behind this thesis is to study the unimolecular reaction of hydrogenated PAH ions in the gas phase under similar states of the interstellar medium (ISM). To achieve such as goal, we decide to study the ion dissociation dynamics of ionized tetralin (1,2,3,4-tetrahydronaphthalene), 9,10-dihydroanthracene ($DHA^{+\bullet}$), 1,2,3,4-tetra- and 1,2,3,4,9,10-hexahydrophenanthrene ($THP^{+\bullet}$ and $HHP^{+\bullet}$) and 1,2,3,4,5,6,7,8-octahydroanthracene ($OHA^{+\bullet}$). A combination of density functional theory and mass spectrometry was used to elucidate the dissociation pathways of each PAH ion. Energies and entropies of activation (E_0, $\Delta^{\ddagger}S$) were derived through RRKM theory. In addition, imaging photoelectron photoion coincidence was used to compare the theoretical and experimental results.

Chapter 2: Techniques

Tandem mass spectrometry (MS) is an analytical technique that can analyze qualitatively and quantitatively chemical samples by measuring the mass-to-charge ratio (m/z) and abundance of gas-phase ions.[34] This method can use a variety of ions sources (chemical ionization (CI), electron ionization (EI), electrospray ionization (ESI), atmospheric pressure chemical ionization (APCI), to name just four), and in this thesis, we used APCI.

2.1. Atmospheric pressure chemical ionization (APCI)

Atmospheric Pressure Chemical Ionization (APCI) is an ionization technique that uses gas-phase ion-molecule reactions at atmospheric pressure.[35] A sample solution is nebulized by the N_2 nebulizer gas and heat (about 400°C) to form a spray, and then sample and solvent molecules are vaporized to a gaseous state. The gaseous solvent (S) and sample (M) are then ionized by a corona discharge, in which a highly charged electrode creates an electric field strong enough to ionize nearby molecules.[36] In this stage, the corona discharge may directly ionize an analyte molecule to form a radical cation ($M^{+\bullet}$) as illustrated in the figure below (**Figure 4**).

$$M + e^- \rightarrow M^{+\bullet} + 2e^- \qquad (1)$$

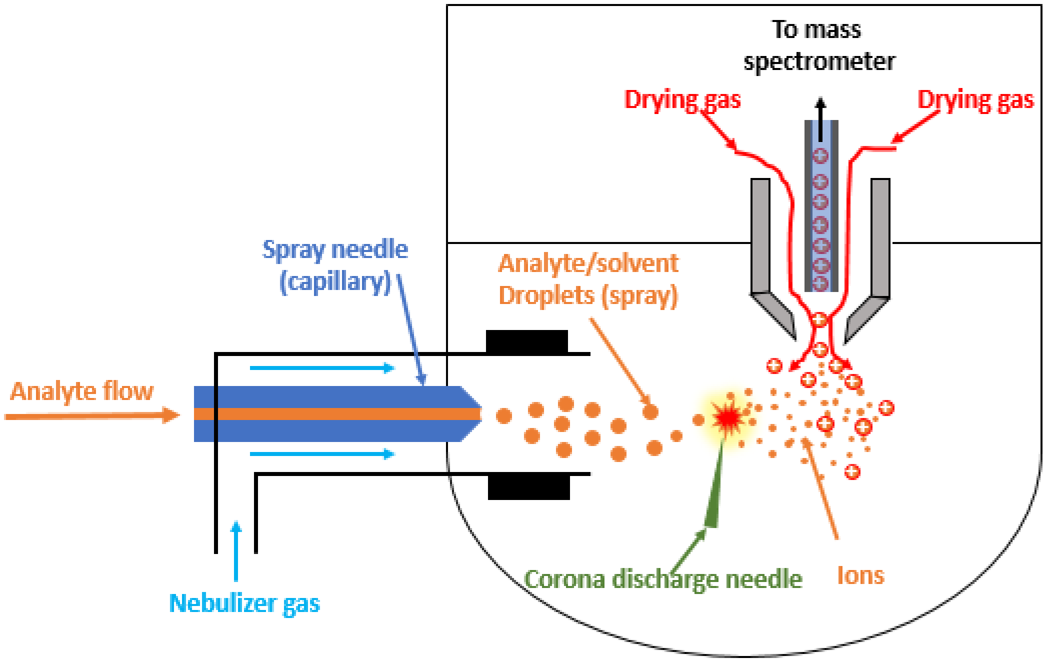

Figure 4. Schematic view of the APCI source.

In the tandem mass spectrometry, the ion source can be matched with a mass analyzer (quadrupole, time of flight, magnetic sector, ion trap or ion cyclotron resonance mass analyzers, to name a few) in order to have the desire products. In our case, the triple quadrupole mass analyzer was used, in which collision-induced dissociation (CID) can be performed.

2.2. Collision Induced Dissociation (CID)

Unlike the single quadrupole systems, the triple quadrupole systems consist of three quadrupoles (Q1 and Q3 are working as mass filters while Q2 is acting as collision cell). Ions generated in the ion source with different m/z enter the first quadrupole that can be set to filter a specific precursor ion of interest, passing that m/z ratio to Q2. The process in the collision cell (Q2) is called collision-induced dissociation (CID) and in it, an adjustable electric field accelerates ions into a neutral gas (usually Ar), with which each ion collides, possibly several times. The kinetic energy of the fast-moving ion is converted to internal energy, therefore increasing the internal energy of the ion to the point that the ion eventually dissociates (**Figure 5**). The resulting fragment ions are finally injected into the third quadrupole where only a specific m/z is allowed to pass. Scanning Q3 results in a CID mass spectrum of the originally selected precursor ion.[37]

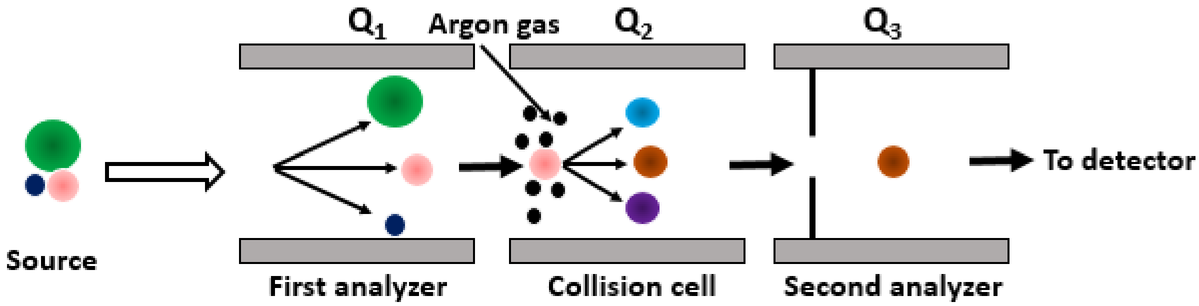

Figure 5. Schematic of triple quadrupole in which different ions entre the Q1 cell but only specific ions (m/z value) are permitted to enter the Q2 (collision cell) and fragment ions are scanned in the Q3 cell.[38]

The motivation behind doing CID, can be analytical, determination of ion structure(s), fundamental studies of properties of ions or any combination.

2.3. Imaging Photoelectron Photoion Coincidence Spectroscopy (iPEPICO)

All the iPEPICO experiments were conducted at the X04DB vacuum ultraviolet (VUV) beamline of the Swiss Light Source (SLS) that is designed to handle ionization event rates in excess of 100 kHz by recording all electron and ion signals (figure 6).[38]

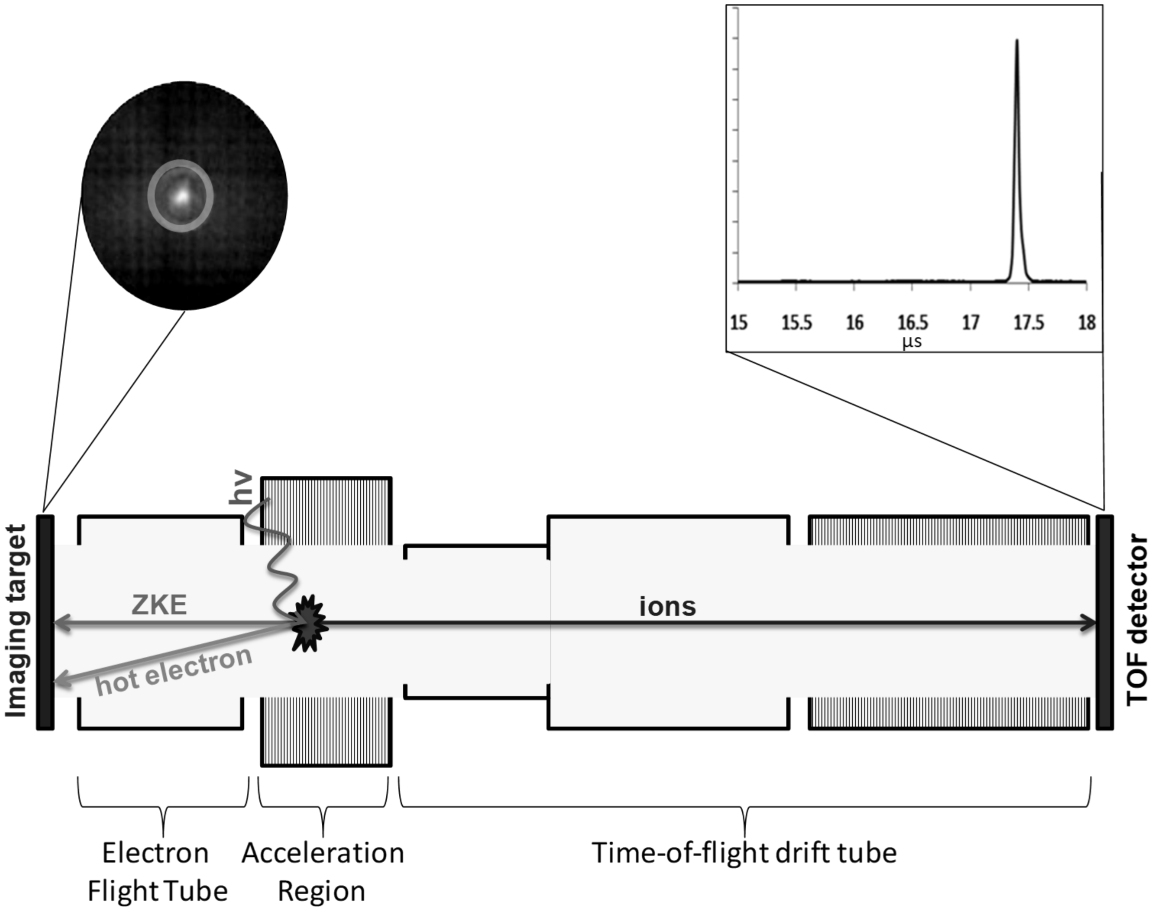

Figure 6. Schematic representation of iPEPICO apparatus. ZKE refers to "zero kinetic-energy electrons", while "hot electron" refers to those made with non-zero kinetic energy.

The iPEPICO apparatus consists of three main components which will be discussed: the ionization and acceleration region, the electron flight tube and detector and the time-of-flight (TOF) mass spectrometer.

The following formula is used to accomplish the iPEPICO experiment that relies on knowing the internal energy of the ion (E_{ion}) within a very small margin.

$$hv = IE_{adia} + E_{ion} + KE \qquad (2)$$

where $h\nu$ is the ionizing photon energy, IE_{adia} is the adiabatic ionization energy and KE is the kinetic energy of the ejected electron.

In this section of the chapter, we describe the main components of this apparatus, which is: the light source, the vacuum system, the electron and ion optics, and the data acquisition system.

2.3.1. Light source

In this region, a copper mirror with platinum reflective coating with a vertical acceptance of 4 mrad and a horizontal acceptance of 8 mrad is used to collimate the bending magnet radiation. Monochromatic light with 10^4 resolving power in the 5–30 eV energy ranges, respectively, is produced by two silicon gratings, with 600 and 1200 mm^{-1} density, that are employed in a constant deviation configuration. The collimated beam is directed with a second mirror onto 110–1000 µm vertical slits in an 80-cm long gas filter, 26 cm from the source. For $h\nu$ <10 eV, a MgF_2 window is used that absorbs virtually all light above 11 eV to avoid double harmonic radiation entering the source. Above the Ne ionization energy, the beamline currently delivers light contaminated by higher harmonics up to $h\nu \approx 140$ eV, which has an intensity to be approximately 10^{11} s^{-1}, depending on the photon energy.

2.3.2. Electron and ion optics

The electrons and ions are accelerated from ground in a 40–250 V cm^{-1} field, between two plates with 10 mm openings, separated by 11 mm. Since a relatively low extraction field is needed to ensure high residence times of the ions in the acceleration region to measure dissociation rate constants, the velocity imaging optics is kept simple, and have not included a magnifying lens to allow for higher fields.[39] Electrons with zero transverse momentum are focused to a less than 1 mm diameter spot at the center of the detector.

The kinetic energy range imaged at the detector depends on the focusing and the flight tube voltages. At a flight tube potential of 147 V, electrons with approximately 400 meV kinetic energy moving perpendicular to the flight axis are imaged at the rim of the active area of the electron detector at 15 mm radius (40 V cm^{-1} extraction field). The energy range can be changed by scaling the extraction field and the corresponding flight tube potential. Each electron event is position and time stamped.

Finally, the iPEPICO apparatus accelerates the ionic fragments within an electric field, thus their kinetic energies are the same and the smaller ions will drift faster than heavier fragments providing time separation. The precursor and fragment ions then arrive at a multichannel plate (MCP) detector where each hit is position and time stamped. The time delay between the arrival of the electron at the imaging target and the detection of the fragment gives the flight time for the fragment ion.

This experiment is repeated many times at a range of photon energies to generate unimolecular breakdown diagrams which will be fit using RRKM theory.

2.4. Computational Methods

2.4.1. Density Functional Theory

Density Functional Theory (DFT) is a computational method that provide information about properties of the molecule based on a determination of the electron density of the molecule. The focus of DFT is the electron density (ρ) and not the wave function as in Hartree-Fock methods. As the energy is a functional of the density, E[ρ], that is why it is given the name of “density functional theory”. A functional is a function of a function, and the energy of the molecule is a functional of the electron density. And this latter is a function with three variables x-, y-, and z-position of the electrons. The mathematics of electron densities and their subsequent correlations to molecular energies is described in the following formula.

$$E_{DFT}[\rho] = T_s[\rho] + E_{ne}[\rho] + J[\rho] + E_{xc}[\rho] \tag{3}$$

with $T_s[\rho]$ the electron kinetic energy, $E_{ne}[\rho]$ the nuclear-electron interaction energy, and $J[\rho]$ the electron-electron interaction energy, and $E_{xc}[\rho]$ is the exchange-correlation energy, which is calculated with an exchange-correlation functional. The choice of this last functional is where different DFT methods diverge and is crucial to the success of the method.[40,41]

To determine the structure, energy is calculated and then the geometry undergoes adjustments and the process is repeated. Then depending on how close the first guess is to the final structure it can either be a local or global minimum of the potential energy surface (PES), the optimized structure is determined within an minimum energy.[42] The minimum energy structures are the stable geometries.

One of the most important things on a surface is the transition state that is defined as the structure associated with a saddle point of the PES (**Figure 7**).

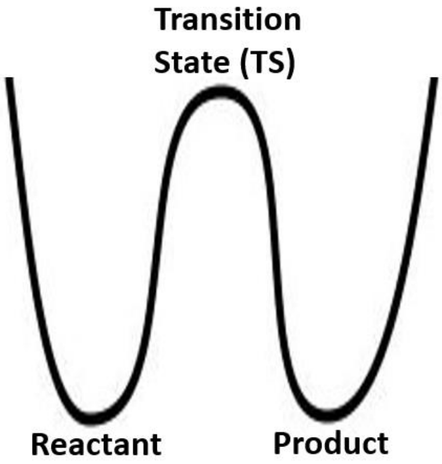

Figure 7. Representative potential energy surface with the location of reactant, transition state and product indicated.[43]

A saddle point is defined as a stationary point (where the first derivative is zero), that is both a maximum and a minimum.[43] For a transition state, the saddle point must be a maximum along only one path, that of the reaction coordinate, while it is a minimum in all other coordinates. Now that the optimized geometries have been defined, the energy corresponding to them must be determined.

Now we can derive the real minimum energy which is used for calculating the reaction energies, such as dissociation energy (ΔE) and ionization energy (IE) by adding to the optimized energy (the electronic energy), the minimum energy of the vibration that is known as the zero point energy (ZPE).[44]

Vibrational frequencies are calculated based on the normal modes of the molecule in the harmonic approximation. The number of vibrational modes is determined based on the degrees of freedom of the molecule without translations and rotations:

$3N - 6$ (non-linear)

$3N - 5$ (linear)

where N represents the number of atoms in the molecule. The calculated frequencies are typically higher in frequency than experiment; therefore, they need to be scaled based on an empirically determined scaling value.[45] The vibrational frequencies calculated can be used to confirm the transition states. The critical frequency, that which leads the molecule to products, will have an imaginary frequency due to the lack of restorative forces on the vibration.[44] The final values derived from the DFT calculations were that of the rotational constants.

The most significant advantage to DFT methods is a significant increase in computational accuracy without the additional increase in computing time, but the challenge is to determine the most appropriate method for a particular application.

2.4.2. Rice–Ramsperger–Kassel–Marcus (RRKM) theory

RRKM theory is a kinetics theory used to estimate unimolecular reaction rates from a few parameters of the potential energy surface. It was developed from the RRK theory by taking Eyring's transition state theory, and the way the various normal-mode vibrations and rotations contribute to reaction, into account. This theory assumes that the rate is proportional to the number of ways of distributing the energy among the internal degrees of freedom of the reactant, so that the critical energy is localized in one particular degree of freedom. It can be a powerful tool for studying gas phase molecular reactions, such as those that occur in planetary atmospheres or in the interstellar medium.[46]

All the reactions discussed in this thesis are unimolecular dissociation reactions of the type,

$$A^{*} \overset{k}{\rightarrow} A^{\ddagger} \rightarrow P \qquad (4)$$

where A* is an excited molecule, k is the rate constant for the dissociation, $A^{\ddagger}$ is the transition state (TS) of A and P are the dissociation products.[47] Based on calculated structures, this theory can be used to calculate the rate of reactions.

RRKM calculates rate constants based on energy, *k(E)*, which was found to be a more versatile methods for calculating rate constants for most chemical systems, especially in the gas phase.[48] RRKM theory is unique in that it includes transition state theory (TST), which makes the assumption that once the reaction reaches the transition state, it proceed to products and never turn back. The following formula is used to calculate *k(E)*,

$$k(E) = \frac{\sigma N^{\ddagger}(E-E_0)}{h\rho(E)} \qquad (5)$$

In this equation, σ represents the degeneracy of the reaction, *h* is Plank's constant, $\rho(E)$ is the density of rotational-vibrational (ro-vib) states of the precursor ion at an internal energy *E* and $N^{\ddagger}(E\text{-}E_0)$ is the number of internal ro-vib states of the transition state at an internal energy of $(E\text{-}E_0)$ with E_0 being the 0 K activation energy. The different energies employed in RRKM theory calculations are illustrated in Figure 8.

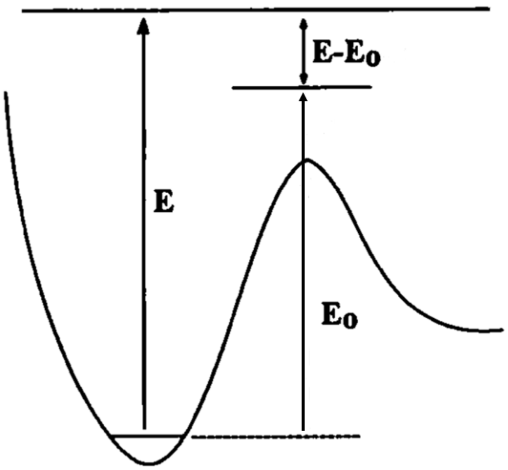

Figure 8. Reaction coordinate for a dissociation with a real barrier.[49]

In this Figure, E and E_0 represent the total ion energy and activation energy and the remaining energy, $E-E_0$ represents the energy available to be statistically distributed among the internal modes of the transition state.[49]

Qualitatively, the sum-of-states represents the number of ways to pass through the transition state that has a total energy of $E-E_0$, while the density of states at an energy E represents the number of ways to get lost in the molecular ion phase space. At this state, we need at least an energy (E_0) and if we have enough energy (E) to overcome this barrier, then we have $E- E_0$ left.

Chapter 3: 1,2,3,4-Tetrahydronaphthalene (Tetralin)

This chapter is reproduced from the following publication: Diedhiou, Malick; West, Brandi; Bouwman, Jordy; Mayer, Paul M, Ion Dissociation Dynamics of 1,2,3,4-Tetrahydronaphthalene: Tetralin as a Test Case For Hydrogenated Polycyclic Aromatic Hydrocarbons, J. Phys. Chem. A, Volume 123, 10885-10892 (2019). 10.1021/acs.jpca.9b09511. The data was acquired by Dr. Brandi West. Jordy Bouwman and Paul Mayer are responsible for the photoelectron spectrum analysis. I worked up the data, did the RRKM fitting of the breakdown and TOF data, did all DFT calculations and analyzed the results.

In light of the results for dihydroPAH ions discussed in the introduction, we have examined the unimolecular reactions of ionized 1,2,3,4-tetrahydronaphthalene, or tetralin, by iPEPICO spectroscopy and tandem mass spectrometry to explore the possibility of H_2 formation from polyhydrogenated precursors. Tetralin, with chemical formula $C_{10}H_{12}$, is one of the smallest superhydrogenated PAHs and is a component of jet[50] and diesel[51] fuels. The unimolecular decomposition of neutral tetralin was previously studied at high temperature under single-pulse shock-tube conditions (1000−1400K) by Tsang and Cui,[52] who determined rates for channels resulting in the formation of ethylene + benzocyclobutene and *o*-allyltoluene. Tetralin is also an intermediate in the synthesis of agricultural chemicals and a good hydrogen donor in the fuel cells.[53-55] So, the question arises if it can be a hydrogen donor in the ISM.

3.1. Experimental methods

3.1.1. Tandem Mass Spectrometry

Atmospheric pressure chemical ionization (APCI) experiments were performed on a Micromass Quattro Ultima (Waters Micromass, Manchester, U.K.) triple quadrupole mass spectrometer equipped with a Z-spray source. Tetralin was purchased from Sigma-Aldrich (Sigma-Aldrich, Oakville, ON, CA, >97% purity) and used without further purification. Compounds were dissolved in chlorobenzene to produce a 100 µg mL^{-1} solution.[56] This solution was delivered to the APCI source by syringe pump at a flow rate of 50 μL min^{-1}. The source block and probe temperatures were 80 °C and 400 °C, respectively, while the corona and cone voltages were 4.0 kV and 40 V. The quadrupole resolution was set to 18 in the Masslynx software to provide baseline separation of all peaks. Collision-induced dissociation (CID) was carried out using argon collision gas at a pressure of approximately 7.8×10^{-4} mbar over a laboratory-frame collision energy (E_{lab}) range of 0 to 31 eV.

3.1.2. Imaging Photoelectron Photoion Coincidence Spectroscopy (iPEPICO)

iPEPICO spectroscopy experiments were conducted on the VUV beamline at the Swiss Light Source (SLS, Paul Scherrer Institut, Villigen, Switzerland) and have been described in detail elsewhere.[38,57,58] Ion optics were adjusted for space-focusing, and thus higher mass resolution, rather than ion imaging. Tetralin was thermally volatilized at 25^{o}C into the photon interaction region with a heated oven and photoionized by monochromatic synchrotron radiation (4−8 meV resolution depending on the photon energy).[59] Electrostatic lenses direct the ions toward a time-of-flight (TOF) mass spectrometer, while the ejected electrons are velocity-mapped on an imaging

RoentDek delay line detector. The electrons are time- and position-stamped at the detector and the corresponding photoions are detected in delayed coincidence. Threshold electrons account for the majority of the signal at the center of the MCP, whereas non-zero-kinetic energy electrons are mostly detected according to their off-axis momentum. Some of the non-zero-kinetic energy electrons will have the proper trajectory to hit the center spot, therefore the mass spectrum based on electrons detected in a ring around the center spot is used to account for this 'hot electron' contamination. The ions detected in coincidence with electrons arriving in the ring can then be subtracted from ions detected in coincidence with the electrons that appeared in the center to obtain the threshold photoionization mass spectrum.[60] The photon energy range used was 10.0 – 13.5 eV, with data points taken every 0.05 eV.

The TOF mass spectrometer consists of two acceleration regions, one with a low draw out potential that allows ions dissociating on the microsecond time scale to do so while being accelerated, resulting in asymmetric time-of-flight peaks for product ions, which can be modeled to extract unimolecular decay rate constants as a function of photon energy. When multiple product ions are generated, they are all formed with the same overall effective decomposition rate constant of the precursor ion, and the fractional fragment ion abundances, i.e., the branching ratios, can be used to apportion absolute dissociation rates to each of the decay channels. This way, dissociation rate constants are obtained for all channels on the basis of the asymmetric peak profile of just one fragment ion.

3.1.3. Computational Methods

Geometry optimizations and harmonic vibrational frequency calculations of all species and transition states were conducted using the Gaussian 16 package[61] at the B3-LYP/6-31+G(d,p) level of theory. Transition states were confirmed with the intrinsic reaction coordinate (IRC) protocol. Franck–Condon simulations utilized the double harmonic approximation.[62] Molecular orbital energies were calculated using the Outer Valence Green's Function Method at the OVGF/cc-pVTZ level of theory.

The minimalPEPICO program was used to fit the iPEPICO breakdown distributions.[57] The program combines the physical parameters of the iPEPICO experimental set up with temperature (for the initial neutral molecule internal energy distribution) and the rate constant for each pathway to calculate theoretical branching ratios for the ion dissociation as a function of photon energy, which are then compared to the experimental breakdown curves. Rice-Ramsperger-Kassel-Marcus (RRKM) theory was used to calculate $k(E)$ according to equation 6,[63,64]

$$k(E) = \frac{\sigma N^{\ddagger}(E-E_0)}{h\rho(E)} \tag{6}$$

where σ represents the reaction degeneracy, h is Planck's constant, $N^{\ddagger}(E - E_0)$ is the number of internal states for the transition state at internal energy $(E - E_0)$ and $\rho(E)$ is the density of states for the reactant ion at internal energy (E). For tetralin, a σ value of 4 was used for $H^{\bullet}$-loss corresponding to the hydrogens bound to the four sp^3 carbon atoms, each $CH_3^{\bullet}$-loss was assigned a value of 1, C_2H_4 loss from the molecular ion was assigned $\sigma = 2$, while that from the isomer (see modeling) was assumed to be 1 and σ for $C_3H_5^{\bullet}$-loss was assigned a value of 1. Rotational-vibrational densities and sums-of-states were calculated using B3-LYP/6-31+G(d,p) rotational constants and harmonic vibrational frequencies by the direct count algorithm of Beyer and Swinehart.[65] The numbers of internal states for the transition state for the reactions were approximated using the vibrational frequencies and rotational constants of the precursor ion, less one vibrational mode to represent the reaction coordinate. Of the remaining 3N − 7 (N = number of atoms) modes for the transition state, the lowest five frequencies were scaled to adjust the entropy of activation. Frequency multiplication factors less than one increase $\Delta^{‡}S$ while values greater than one decrease $\Delta^{‡}S$.[63] The agreement between the experimental and theoretical breakdown curves was achieved by varying E_0 and $\Delta^{‡}S$. Error bars were established by finding the limits in E_0 and $\Delta^{‡}S$ that resulted in a value of < 5 % for equation 7:

$$Difference = 1 - \frac{\Sigma((Expt)(Calc))}{\sqrt{\left(\Sigma((Expt)(Expt))\Sigma((Calc)(Calc))\right)}} \qquad (7)$$

where *Expt* and *Calc* refer to the experimental and calculated relative ion abundances in the breakdown curves, respectively.

3.2. Results and Discussion

3.2.1. Threshold photoelectron spectrum

The mass-selected threshold photoelectron spectrum (TPES) of tetralin was acquired from 8.3 – 15.5 eV with steps of 0.001 eV to establish the ionization energy, Fig. 9. The TPES exhibits a sharp first ionization band from which an ionization energy (IE) value of 8.46 ± 0.01 eV is derived. A simulated ionization spectrum is constructed using the program eZspectrum by considering the overlap between the vibrational wavefunctions in the ground state neutral tetralin with those in the ground state of the cation. The simulated spectrum is shown in the inset in Fig. 1 both as a stick diagram as well as a spectrum that results from a convolution of the stick diagram with Gaussian shape with a Full-Width-at-Half-Maximum of 30 meV (250 cm^{-1}). All of the main vibronic resonances observed in the experimental spectrum are accounted for by the simulations. There is a mismatch between the measured and simulated spectrum at an energy between 8.9 and 9.1 eV, which is due to an electronically excited state in the tetralin cation. OVGF calculations were used to locate tetralin ion excited states and the results are overlaid on the TPES in Fig.9, and listed in table 1.

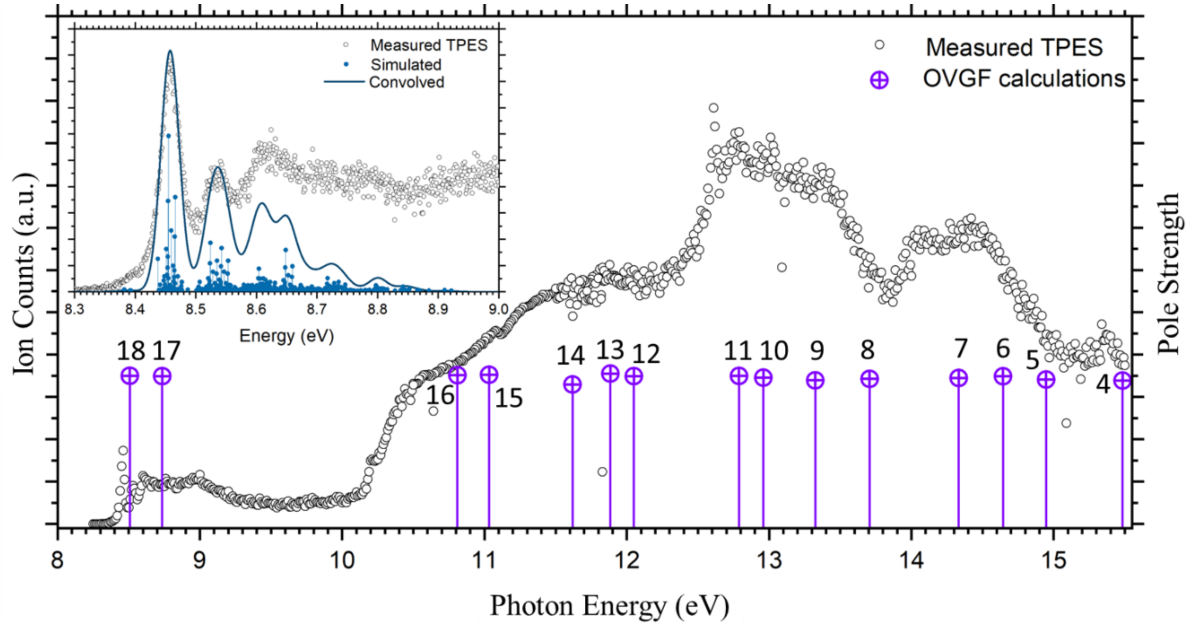

Figure 9. Overview of the TPES of tetralin to 16 eV, with OVGF results. The inset holds an expansion of the threshold region together with a Franck-Condon simulated spectrum. The simulated spectrum is displayed both as a stick diagram, as well as a spectrum that results from a convolution of the stick spectrum with a 30 meV FWHM Gaussian line shape.

Table 1. Comparison of the experimental and OVGF/cc-pVTZ molecular orbital vertical ionization energies.

MO	Orbital Vertical IE (eV)		PS*
	TPES	OVGF	
1		18.155	0.854
2		16.489	0.854
3		15.483	0.865
4		15.709	0.876
5	15.2	14.946	0.871
6	14.5	14.643	0.89
7	14.0	14.332	0.88
8	13.5	13.706	0.875
9	13.0	13.324	0.866
10	12.8	12.959	0.882
11	12.6	12.788	0.892
12	10.0 - 12.0	12.049	0.891
13		11.884	0.906
14		11.618	0.842
15		11.032	0.899
16		10.809	0.896
17	8.9	8.735	0.891
18	8.46 ± 0.01	8.507	0.893

* Pole Strength

3.2.2. Collision-induced dissociation (CID)

The CID breakdown graph for ionized tetralin is shown in Fig. 10.

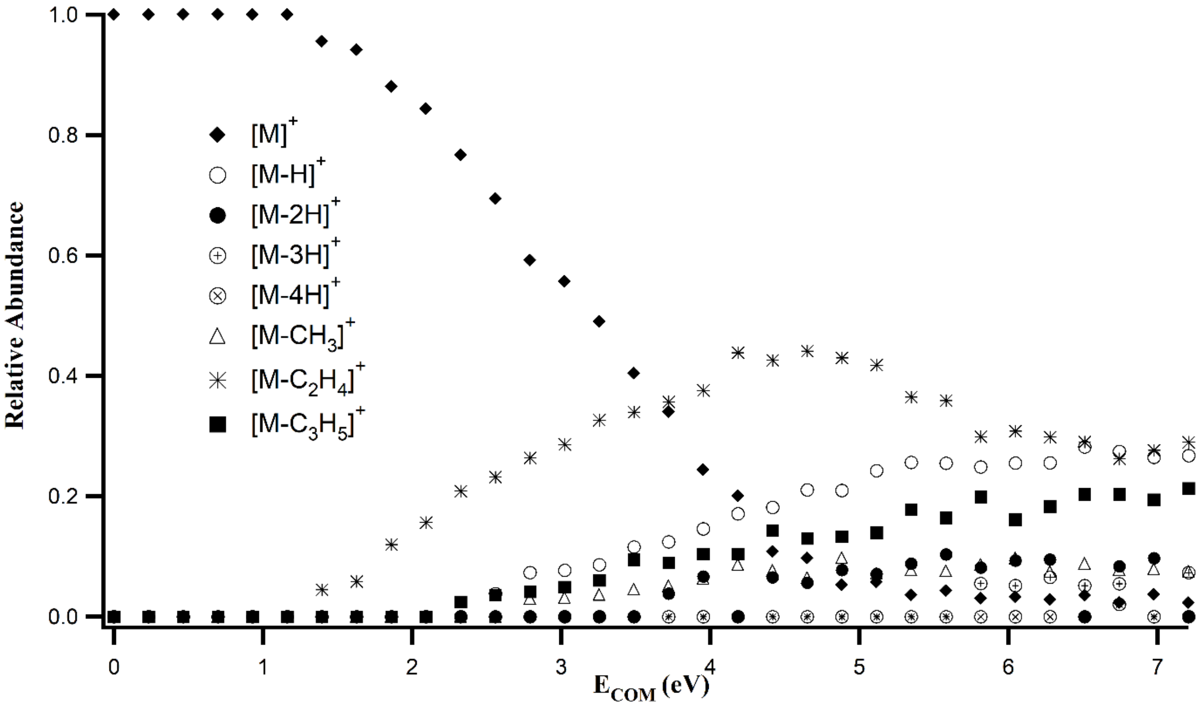

Figure 10. CID breakdown graph for ionized tetralin.

The decomposition of tetralin leads to loss of hydrogen atoms (sequential loss of up to 4 H atoms) and hydrocarbon units ($CH_3^•$, C_2H_4 and $C_3H_5^•$); however, the most significant process are loss of $H^•$, $CH_3^•$, C_2H_4 and $C_3H_5^•$ (reactions R1 – R4), the others accounting for less than 10% of the total fragmentation at high collision energy (and of this -2 H is the predominant process).

$C_{10}H_{12}^{•+} \rightarrow C_{10}H_{11}^+ + H^•$ (*m/z* 131) (R1)

$C_{10}H_{12}^{•+} \rightarrow C_9H_9^{•+} + CH_3^•$ (*m/z* 117) (R2)

$C_{10}H_{12}^{•+} \rightarrow C_8H_8^{•+} + C_2H_4$ (*m/z* 104) (R3)

$C_{10}H_{12}^{•+} \rightarrow C_7H_7^+ + C_3H_5^•$ (*m/z* 91) (R4)

Based on the sequential appearance of the $–H^{•}$ and $–2H^{•}$ peaks in the breakdown graph, we conclude that $[M–2H]^{•+}$ is due to a step-wise loss of two H atoms rather than loss of H_2.

3.2.3. VUV-induced dissociation

The major fragmentation pathways R1-R4 are also observed in the iPEPICO data (Fig. 11a), with the addition of a small peak with m/z 128 that can only be due to loss of 4 $H^{•}$-atoms, presumably leading to ionized naphthalene. Originally thought to be an artifact, this ion is reproducible and is also observed in the 70 eV electron ionization mass spectrum of tetralin.[66] The lack of this peak in the CID mass spectra, except at high collision energy after loss of three H atoms, enforces the idea that this channel in the iPEPICO experiment is possibly from a non-statistical process of the molecular ion (vide infra). The assumption that unimolecular reactions are driven by statistical dynamics is at the heart of transition state theory. So, to model the iPEPICO breakdown curves, we first removed this minor $[M-4H]^{•+}$ peak (Fig. 11b). Representative time-of-flight distributions are shown in Fig. 11c.

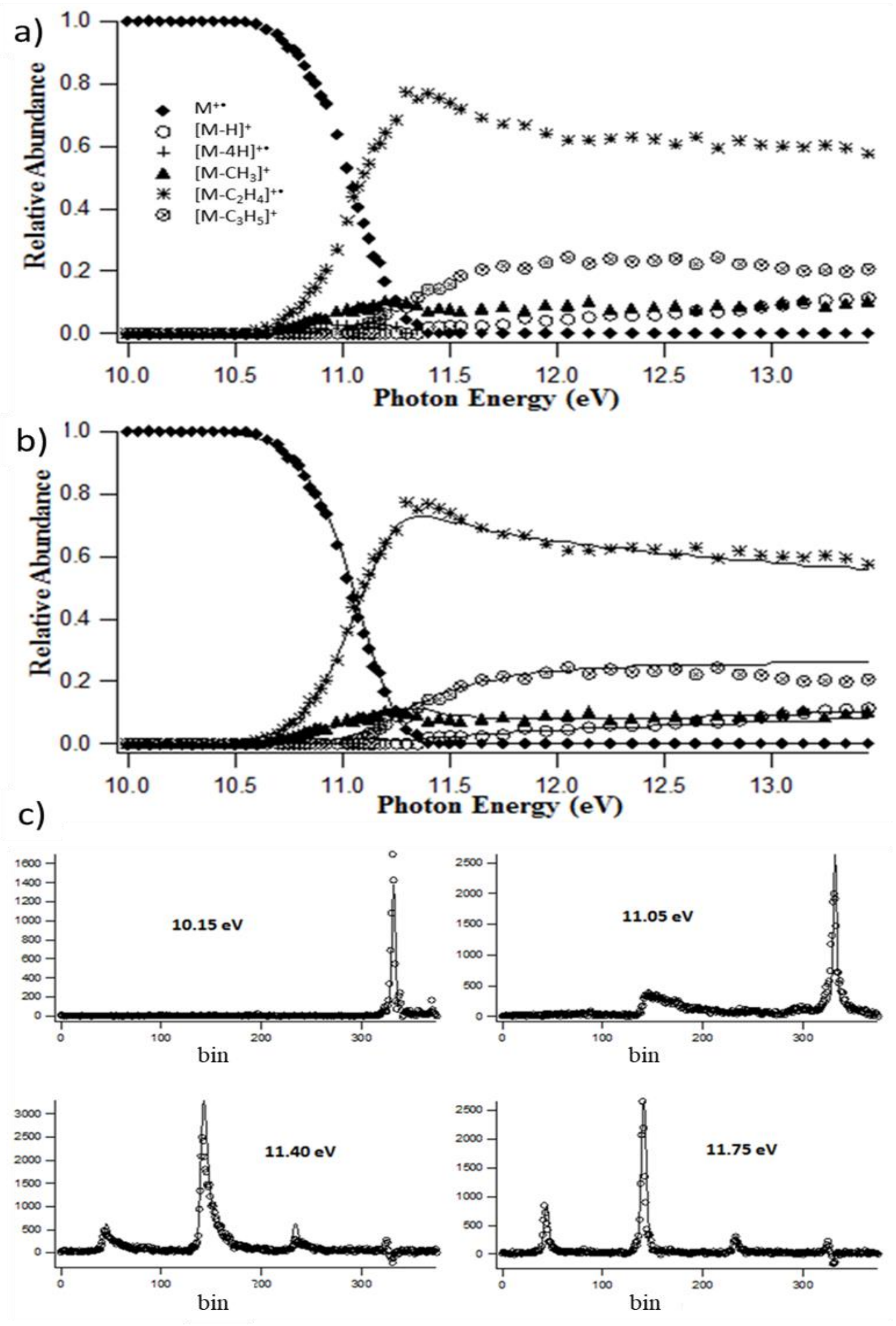

Figure 11. a) iPEPICO breakdown diagram of tetralin with 4H•-loss, b) RRKM (solid line) modeled iPEPICO breakdown curves ([M-4H]•+ ion removed), c) asymmetric time-of-flight distributions (with RRKM fit) at four representative photon energies.

3.2.4. RRKM modeling

RRKM modeling of the curves in Fig. 11b, c (solid lines through the experimental points) could only be achieved by assuming a 2-well potential energy surface. This type of surface is consistent with what was required in the case of dihydronaphthalene and dihydrophenanthrene as methyl loss in those two cases required isomerization of the molecular ions to methylindene ions (and its analogue for dihydrophenanthrene).[33] In addition, it was clear that there had to be two distinct sources for $[M\text{-}C_2H_4]^{\bullet+}$ and $[M\text{-}CH_3^{\bullet}]^+$, and so the resulting, experimentally derived surface is shown in Fig. 12. The isomerization barrier governs the branching ratio between the two pathways to $[M\text{-}C_2H_4]^{\bullet+}$ and $[M\text{-}CH_3^{\bullet}]^+$, and so the uncertainties on the reaction energies for forming these products from the isomer will be significant.

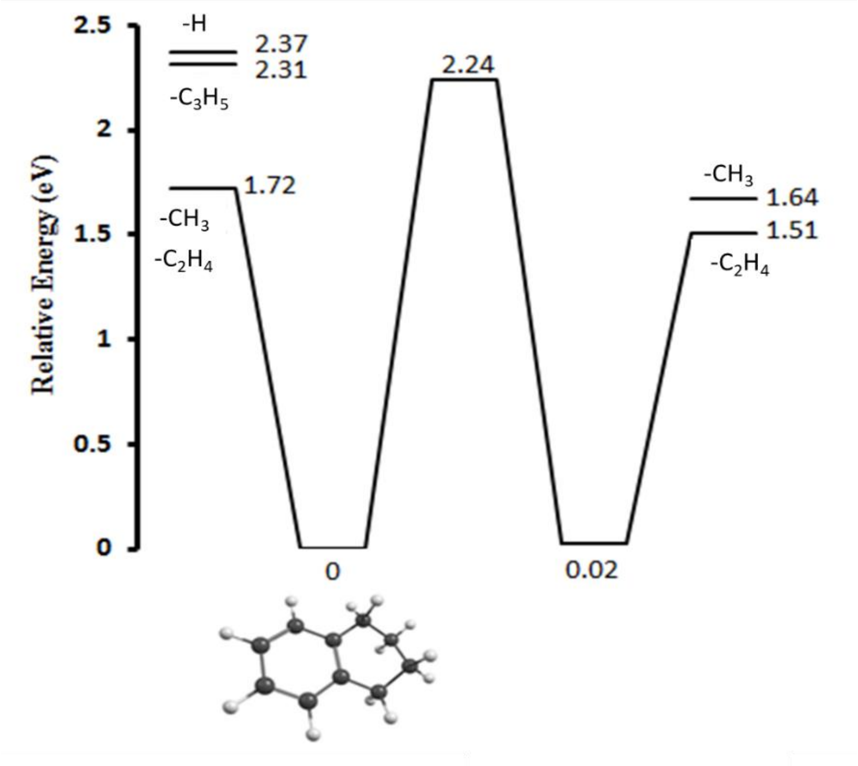

Figure 12. Two-well reaction model used for the RRKM fit to the experimental data. All energies obtained from the fitting procedure.

3.3. Computational Results

$CH_3^{\bullet}$-loss. The most logical source for methyl radical loss is from methylindane, analogous to the loss of $CH_3^{\bullet}$ from methylidene in the case of dihydronaphthalene.[33] We found a direct isomerization pathway to 1-methylindane, which then leads to the loss of a methyl radical (Fig. 13). Both the isomerization energy of 2.45 eV and bond cleavage energy of 1.25 eV are consistent with those derived from the RRKM fitting of the iPEPICO data (2.24 and 1.64 eV, respectively, given the expected high uncertainty in the latter quantity).

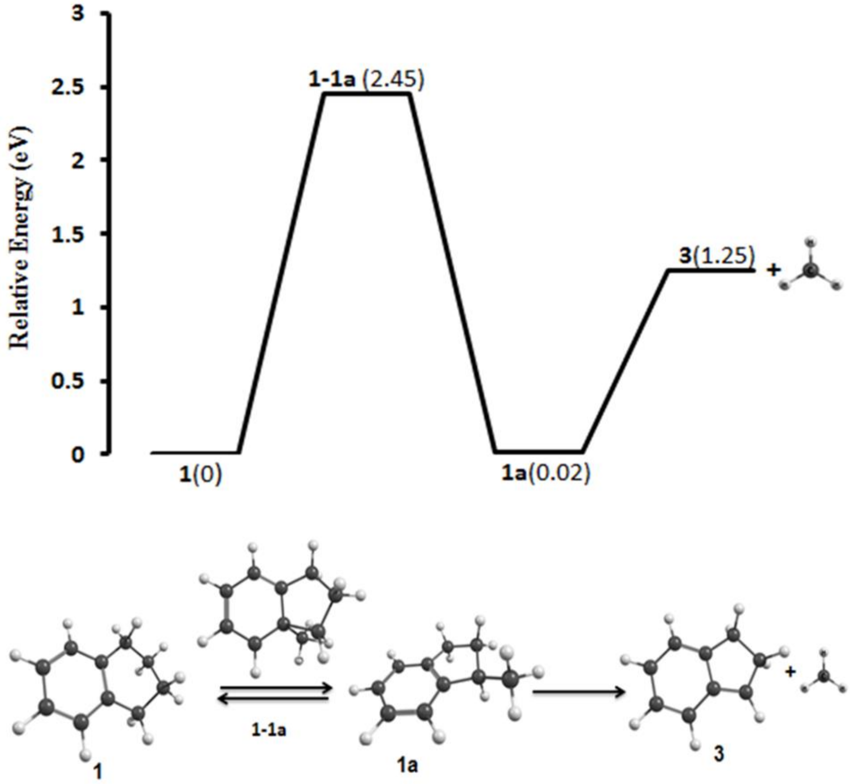

Figure 13. Potential energy surfaces for CH3•-loss from ionized tetralin via 1-methylindane computed at the B3LYP/6-31+G(d,p) level of theory.

Methyl-loss from the molecular ion can occur via the pathway described in Fig. 14. It involves hydrogen migration prior to ring opening to form **1d**. Hydrogen migration in the newly-formed side chain can lead to the formation of allyl benzene (**4**).

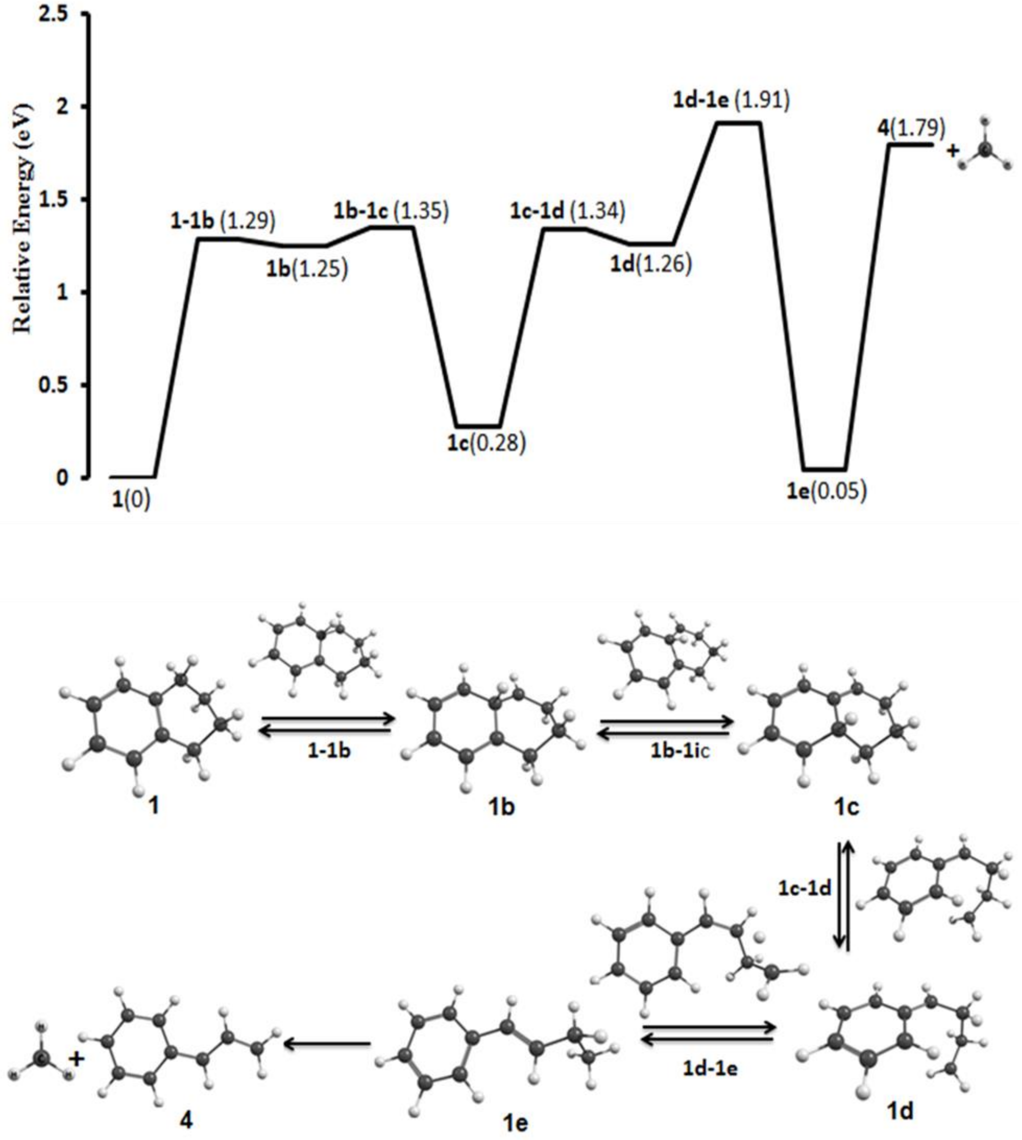

Figure 14. Potential energy surfaces for CH3•- loss from ionized tetralin computed at the B3LYP/6-31+G(d,p) level of theory.

C_2H_4-loss. Unlike PAH ions which lose C_2H_2,[67,68] and dihydroPAH ions which do not exhibit a 2-carbon loss channel,[33] tetralin starts to behave more like a regular hydrocarbon and loses C_2H_4. It does so in two distinct channels, one from the molecular ion and one from the 1-methylindane isomer. A mechanism for C_2H_4-loss from the molecular ion is shown in Fig. 15 and the energy required to generate the ethenylbenzene radical cation **5** is 1.40 eV. The key intermediate in this reaction, **1i**, is formed by hydrogen migration to the opposite bridging carbon.

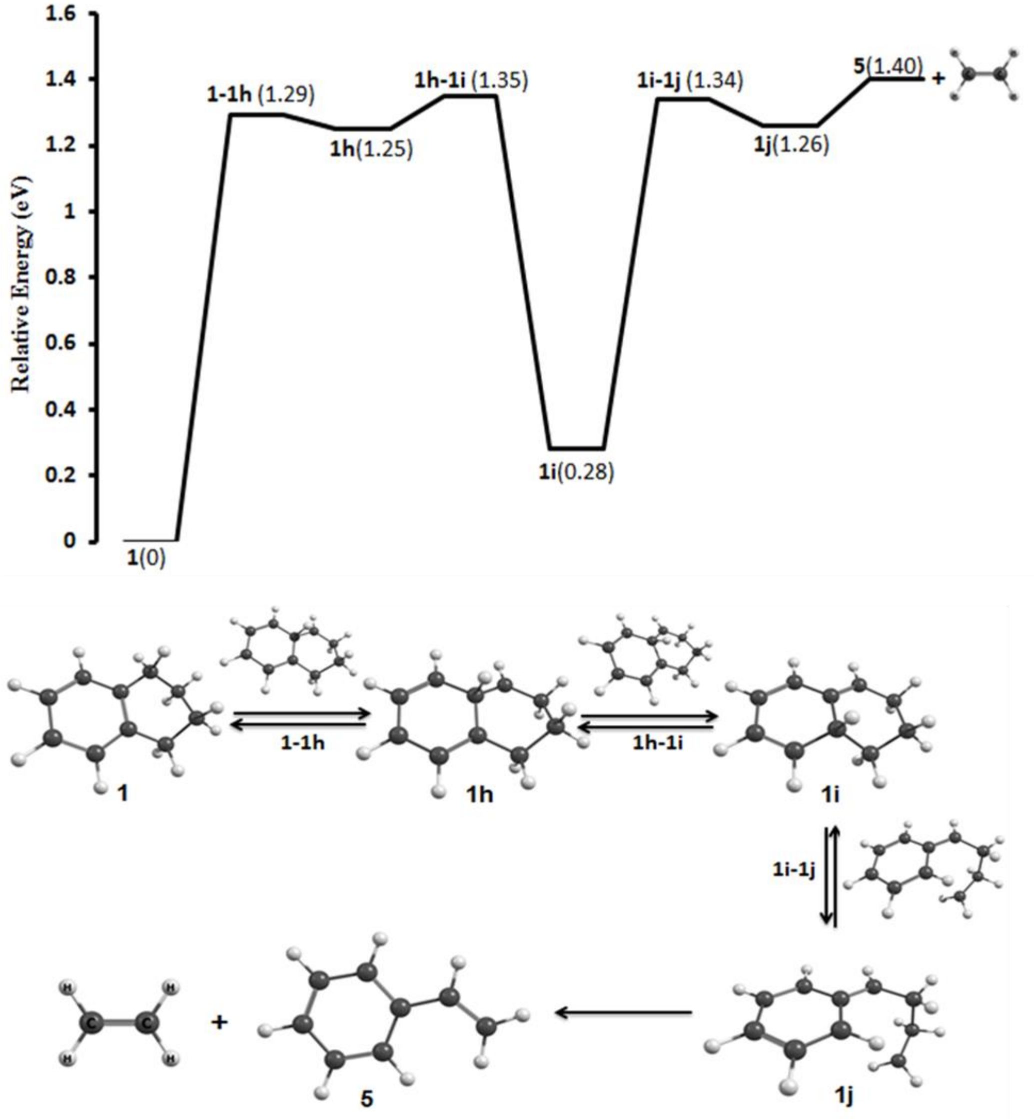

Figure 15. Route for C2H4-loss from ionized tetralin at the B3LYP/6-31+G(d,p) level of theory.

C_2H_4-loss from the 1-methylindane ion (**1f**) also generates ionized ethenylbenzene **5** but requires 1.99 eV (Fig. 16). This pathway is formed via a ring-opening reaction on the hydrated ring. Given the high energy of TS(**1q-1r**), it would at best be a minor contributor to the C_2H_4-loss channel.

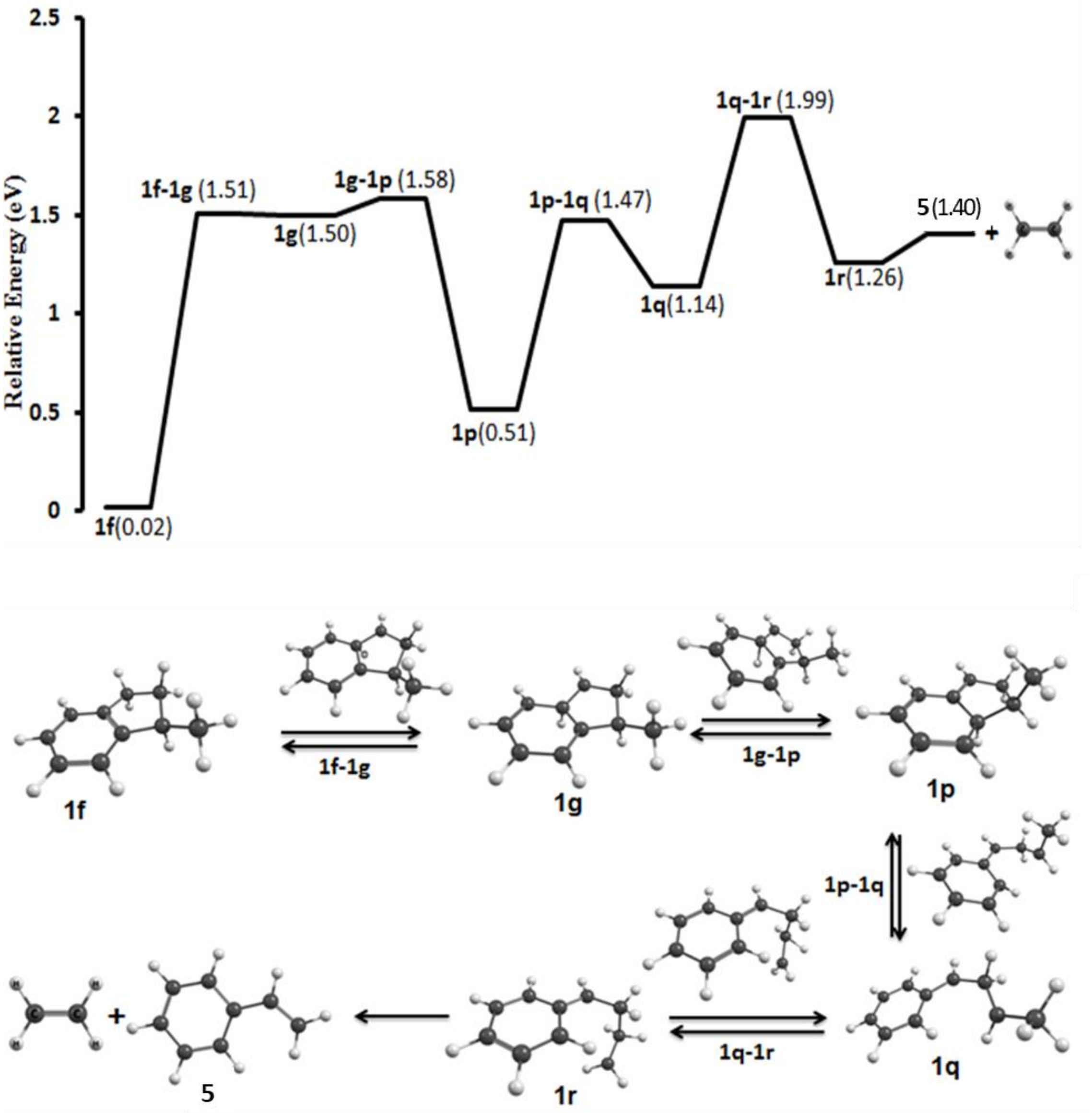

Figure 16. Pathway for C2H4-loss from ionized 1-methylindane (calculated at the B3LYP/6-31+G(d,p) level of theory).

Unlike napthalene ions,[69] it does not appear necessary to go through a partially hydrogenated azulene intermediate and form a dihydropentalene isomer. Three key intermediates for such a process lie 2.07, 2.01 and 2.68 eV relative to the tetralin ion.

$C_3H_5^\bullet$-loss. Two possible channels leading to the loss of the allyl radical exist. First, the loss of the allyl radical to generate the tropylium ion (**6**), the lowest energy product ion, is shown in Fig. 17. The highest barrier on this surface has an energy of 2.72 eV, significantly higher than the 2.31 eV derived from the RRKM model. Secondly, formation of the benzyl cation (**7**) requires only 2.10 eV (Fig. 18), which is more consistent with the experimentally-derived value, and so this could be a case that the thermodynamically-most favoured product is not the kinetically-favoured one.

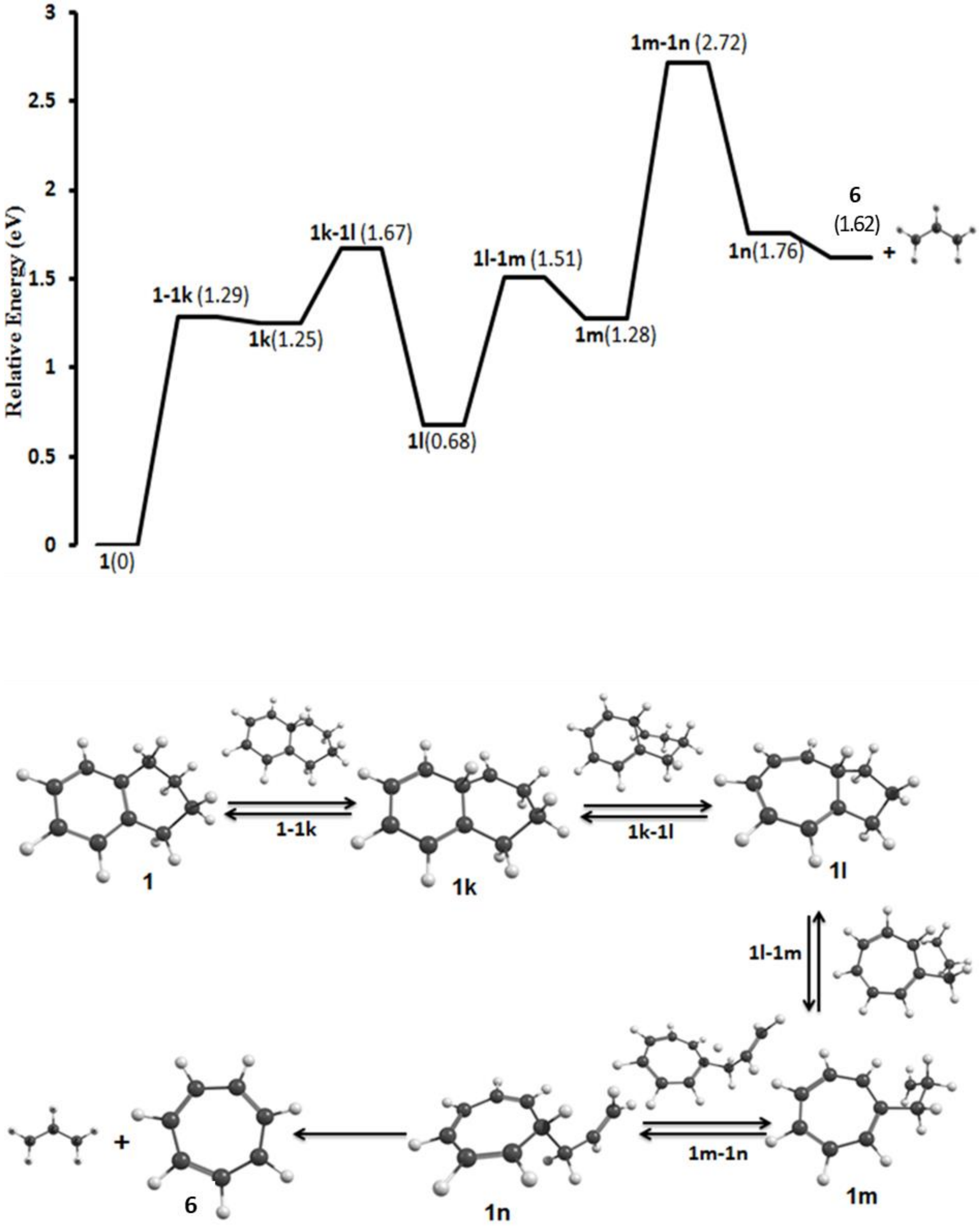

Figure 17. Potential energy surfaces for C3H5•-loss to form the tropylium ion 6 from ionized tetralin, computed at the B3LYP/6-31+G(d,p) level of theory. There must be a barrier between 1n and products, but we were unable to optimize this structure.

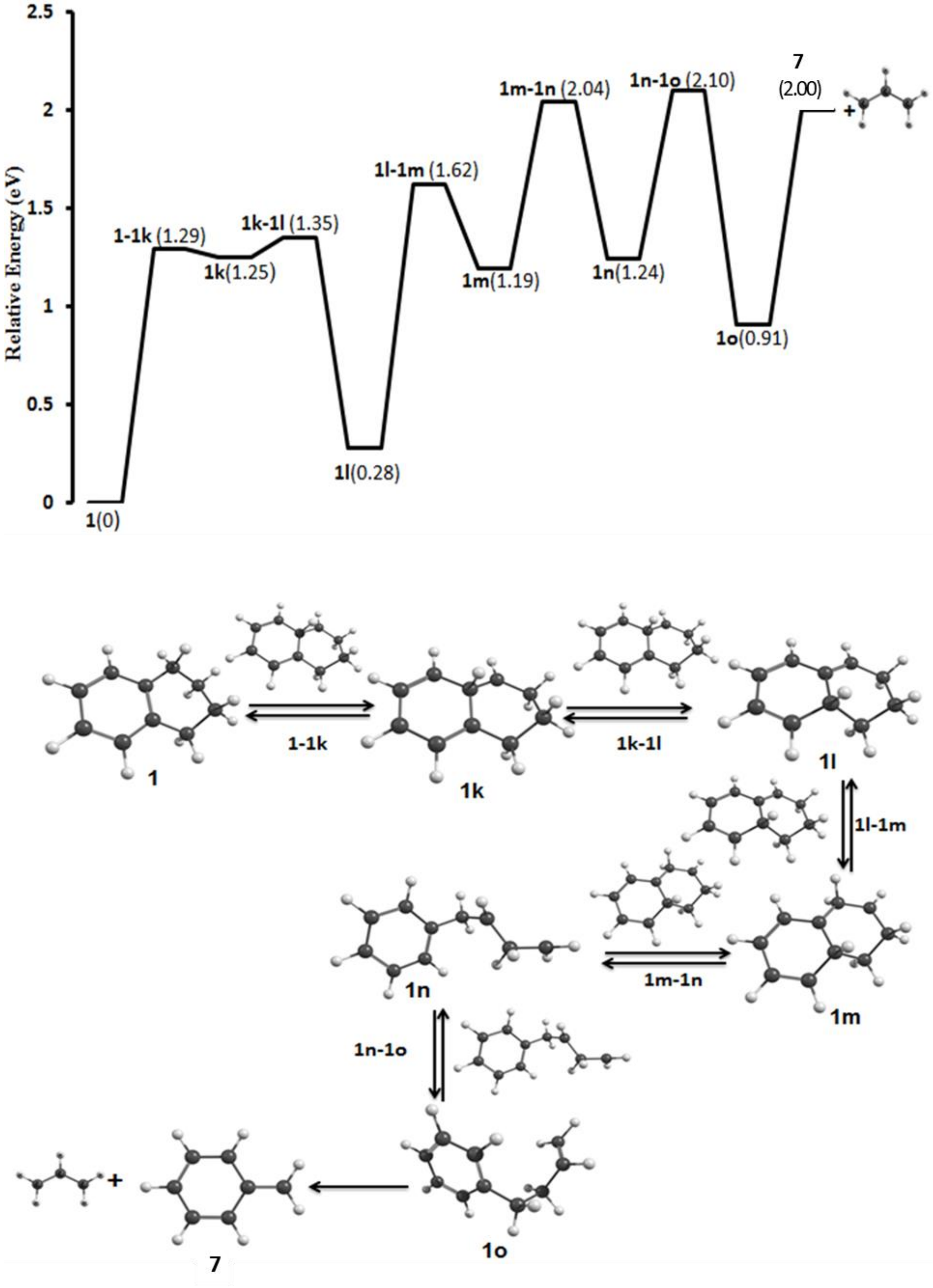

Figure 18. Potential energy surfaces for C3H5•-loss to form the benzyl cation 8 from ionized tetralin, computed at the B3LYP/6-31+G(d,p) level of theory.

H$^\bullet$ atom loss. Simple H$^\bullet$-loss from ionized tetralin from the 1 or 4 position on the hydrated ring has a minimum energy requirement of 1.90 eV computed at the B3LYP/6-31+G(d,p) level of theory. No reverse barrier was found from a relaxed potential energy surface scan at the B3LYP/6-31G(d) level of theory. The energy required to remove one of the H$^\bullet$ atoms from positions 2 or 3 raises to 2.56 eV, while from the unsaturated ring H loss was calculated to be 4.26 and 4.42 eV (positions 5 and 6 respectively), similar to what one expects from ionized PAHs.[68] H$^\bullet$ atom loss also likely occurs from the methylindane isomer, but the low abundance of the peak in the data made it unnecessary to include a second channel in the RRKM fitting. This latter H$^\bullet$-loss reaction was calculated to have an energy requirement of 1.9 eV at the B3LYP/6-31+G(d,p) level of theory.

Chapter 4: Larger Hydrogenated PAHs

This chapter is reproduced from the following publication, that is currently in the revision stage: Diedhiou, Malick; West, Brandi; Mayer, Paul M, How Does Successive Hydrogen Addition to PAH Ions Impact Their Unimolecular Chemistry? Mol. Astrophys., MOLAP-D-19-00015 (submitted December 2019). The data was collected at the Swiss Light Source by B. West and P. Mayer. I worked up the data, did the RRKM fitting of the breakdown and TOF data, did all DFT calculations and analyzed the results for dihydroanthracene and octahydroanthracene. The two hydrophenanthrenes were explored by P. Mayer.

In this study we are exploring the trends in unimolecular reaction pathways as hydrogen is added to a hydrogenated PAHs, notably going from di- to octa-hydroanthracene and from tetra- to hexa-hydrophenanthrene, to probe the conversion from PAH ion chemistry to that of cyclic saturated hydrocarbon ions like cyclohexane or decahydronapthalene.

4.1. Experimental Methods

9,10-Dihydroanthracene (DHA), 1,2,3,4,5,6,7,8-octahydrohanthracene (OHA), 1,2,3,4-tetrahydrophenanthrene (THP) and 1,2,3,4-9,10-hexahydrophenanthrene (HHP) were obtained from Sigma-Aldrich (Sigma-Aldrich, Oakville, ON, CA). It became clear during the measurements that the sample of HHP was impure, containing a significant contribution of THP, Figure 19.

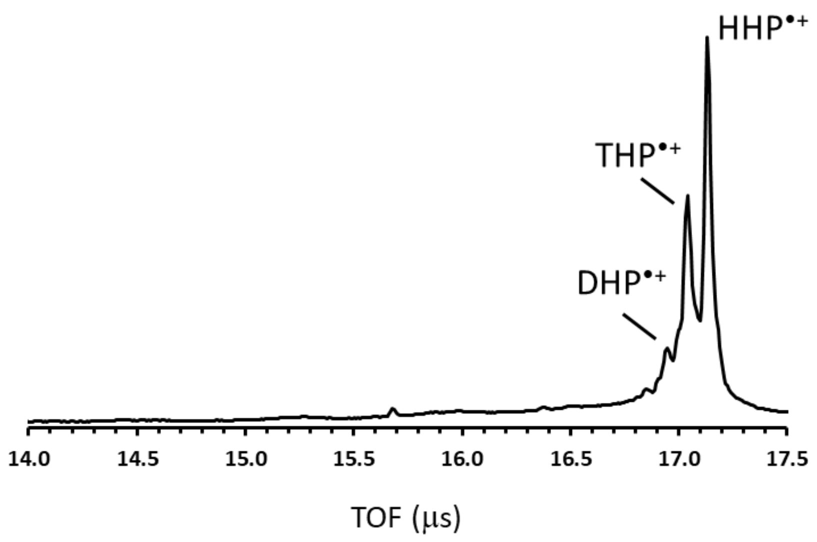

Figure 19. Uncorrelated iPEPICO mass spectrum of the HHP sample at 10.6 eV. Visible are a major contribution from THP and a minor contribution from DHP impurities.

4.1.1. Tandem Mass Spectrometry

Atmospheric pressure chemical ionization (APCI) experiments were performed on a Micromass Quattro Ultima (Waters Micromass, Manchester, U.K.) triple quadrupole mass spectrometer. Compounds were dissolved in chlorobenzene (100 μg mL^{-1}) according to the protocol established by Vaikkinen and co-workers [56] and delivered to the source by syringe pump and a rate of 50 μL min^{-1}. Instrumental parameters were: source block (80°C) APCI probe (400°C), corona needle (4.0 kV) and sampling cone (40 V). Baseline separation of mass spectral peaks was achieved by setting the quadrupole resolution to 18 in the Masslynx software. Collision-induced dissociation (CID) was carried out using argon collision gas (8 × 10^{-4} mbar).

4.1.2. Imaging Photoelectron Photoion Coincidence Spectroscopy (iPEPICO).

iPEPICO spectroscopy experiments were conducted on the VUV beamline at the Swiss Light Source (SLS, Paul Scherrer Institut, Villigen, Switzerland) and have been described in detail elsewhere [38,57,58], and specifically discussed by our group in a series of publications [33,68,70-78] and so only a short description will be provided here. Samples were thermally volatilized into the photon interaction region with a heated oven and photoionized by monochromatic synchrotron radiation [59]. Ions and ejected electrons are detected in delayed coincidence, the latter with an imaging detector. Threshold electrons are preferentially detected at the center of the imaging detector and the ions detected in coincidence with these electrons make up the energy-resolved mass spectra. Ions formed in coincidence with non-zero-kinetic energy electrons that manage to hit the centre spot on the detector are subtracted from the threshold mass spectrum [60].

The threshold photoelectron spectrum (TPES) of DHA was previously reported [79] and produced an IE of 8.335 ± 0.010 eV. The TPES for OHA, Figure 20a, was acquired from 7.8 – 8.2 eV with steps of 0.01 eV to establish an IE of 7.89 ± 0.02 eV, a minor update to the 1980 value by Meot-Ner of 7.86 ± 0.05 eV, based on high-pressure mass spectrometry ion-equilibrium meaurements [80]. The TPES of THP, Figure 20b, yielded a new IE of 7.74 ± 0.01 eV. The TPES of HHP had two bands, one at 7.57 ± 0.01 eV corresponding to the ionization of HHP and one at 7.74 eV corresponding to the THP impurity.

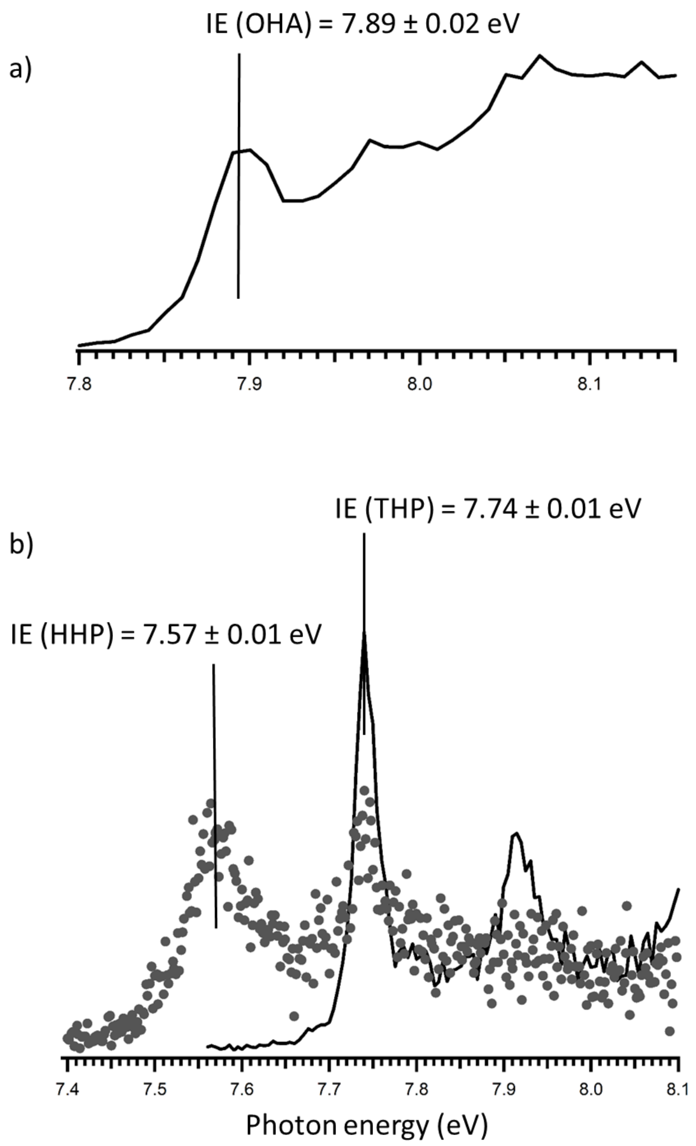

Figure 20. Threshold photoelectron spectra of a) OHA and b) THP (solid line) and HHP (dots), the latter showing the THP impurity.

The TOF mass spectrometer consists of two acceleration regions, the first of which has a low draw-out potential. Ions dissociating in this region give rise to asymmetric TOF distributions that reflect the net dissociation rate constant of the precursor ion. Branching ratios can then be used to apportion absolute dissociation rates to each of the product ion channels.

Since the mass resolution of the TOF mass spectrometer is quite low, it was necessary to use a deconvolution procedure to distinguish the precursor ion from $H^{\bullet}$-atom loss fragments when plotting the breakdown curves for the ions. The procedure finds the weighted center of the $M^{+\bullet}$ and $[M\text{-}H]^{+}$ region TOF distribution [78]. $M^{+\bullet}$ has a peak with a certain TOF centre and width. As the $[M\text{-}H]^{+}$ peak grows with increasing photon energy, the center of the TOF distribution of the peak cluster shifts towards the TOF of the $[M\text{-}H]^{+}$ ion, the shift being proportional to the relative abundance of the two peaks. This analysis is unnecessary when comparing experimental and theoretical TOF distributions.

4.1.3. Computational Methods

Geometry optimizations and harmonic vibrational frequency calculations of all species and transition states employed the B3-LYP/6-31+G(d,p) level of theory in the Gaussian 16 suite of programs [61]. Transition states were confirmed with the intrinsic reaction coordinate (IRC) protocol.

The minimalPEPICO program was used to fit the iPEPICO breakdown distributions [57], and has also been described extensively in our previous publications. The program combines the physical parameters of the iPEPICO experimental set up with temperature (for the initial neutral molecule internal energy distribution) and the rate constant for each pathway to calculate theoretical branching ratios and TOF distributions for the ion dissociation as a function of photon energy, which are then compared to the experimental breakdown curves and mass spectra. The symmetry values employed in the RRKM modeling are summarized in Table 1.

Table 2. Symmetry values for the RRKM calculations of each reaction.

Reaction	σ	
DHA – H	2	Two low energy sites in the molecular ion.
DHA – H (from isomer)	1	In the isomer, there is only one route to each product.
DHA – CH_3 (from isomer)	1	
OHA - H	8	Reactions can occur from either side of the molecule.
OHA – C_2H_4	4	
OHA – C_3H_5	2	
THP – H (from isomer)	1	In the isomer, there is only one route to each product.
THP – CH_3 (from isomer)	1	
THP – C_2H_4	2	} Based on tetralin.
THP – C_3H_5	1	
HHP – H (from isomer)	1	In the isomer, there is only one route to each product.
HHP – CH_3 (from isomer)	1	
HHP – C_2H_4	2	} Based on tetralin.
HHP – C_3H_5	1	
HHP – C_4H_6	1	

4.2. Results and Discussion

The iPEPICO and CID derived breakdown curves for DHA$^{+\bullet}$, OHA$^{+\bullet}$ and THP$^{+\bullet}$ are presented in Figure 21 and representative time-of-flight (TOF) distributions as a function of photon energy for all four molecules are found in Figures 22-25 In the case of HHP$^{+\bullet}$, the THP impurity made it impossible to separate out the individual reactions in order to construct a breakdown diagram for HHP$^{+\bullet}$. The breakdown curve for DHA$^{+\bullet}$ is characterized by a low-slope decrease of the molecular ion relative abundance and the loss of $H^\bullet$ and $CH_3^\bullet$, as was observed for 1,2-dihydronapthalene and 9,10-dihydrophenanthrene [33], The same behaviour is seen in the CID breakdown curves, Figure 21a. In the case of OHA$^{+\bullet}$ only $H^\bullet$, C_2H_4 and $C_3H_5^\bullet$ neutral loss pathways are observed in the iPEPICO experiment, although the CID results also show minor reactions leading to loss of $CH_3^\bullet$, Figure 21b. In this respect, the CID results are consistent with previous work on tetralin, another hydrogenated PAH with four saturated carbon atoms on one ring [71]. However, for OHA$^{+\bullet}$, the very minor $CH_3^{\bullet}$ loss channel seen in the CID data no longer competes on the shorter timescale iPEPICO experiment, and is not observed, leaving only the $H^{\bullet}$, C_2H_4 and $C_3H_5^{\bullet}$ neutral loss pathways.

The iPEPICO breakdown curves for $THP^{+\bullet}$ exhibit all four reactions: loss of $H^{\bullet}$, $CH_3^{\bullet}$, C_2H_4 and $C_3H_5^{\bullet}$. There was a large degree of uncertainty in the ratio of the molecular ion to that for $H^{\bullet}$ atom loss due to the lack of mass resolution and poor signal strength. This made the centre-of-mass analysis, required to separate the contribution of these two ions to the mass spectrum, unreliable, resulting in significant scatter in the breakdown curves of those two peaks. It is the reason why the RRKM fit to the curves (solid lines) misses the molecular ion peak above 12 eV. Thus, more emphasis was placed on fitting the experimental TOF distributions in Figure 24 than on the breakdown curves. $HHP^{+\bullet}$ also displays $H^{\bullet}$, $CH_3^{\bullet}$, C_2H_4 and $C_3H_5^{\bullet}$ formation, plus loss of C_4H_6 at higher photon energies, Figure 25. RRKM fitting was achieved solely through the use of the TOF distributions, Figure 25. In this case, the RRKM derived TOF distributions for $THP^{+\bullet}$ were combined with those for $HHP^{+\bullet}$ in order to match the experimental data.

In summary, we observe a trend in reactivity in going from $DHA^{+\bullet}$ to $THP^{+\bullet}$, $HHP^{+\bullet}$ and ultimately $OHA^{+\bullet}$ which sees decreasing abundance of $H^{\bullet}$ and $CH_3^{\bullet}$-loss and an increasing dominance of the formation of C_2H_4, $C_3H_5^{\bullet}$ and higher hydrocarbons with degree of hydrogenation.

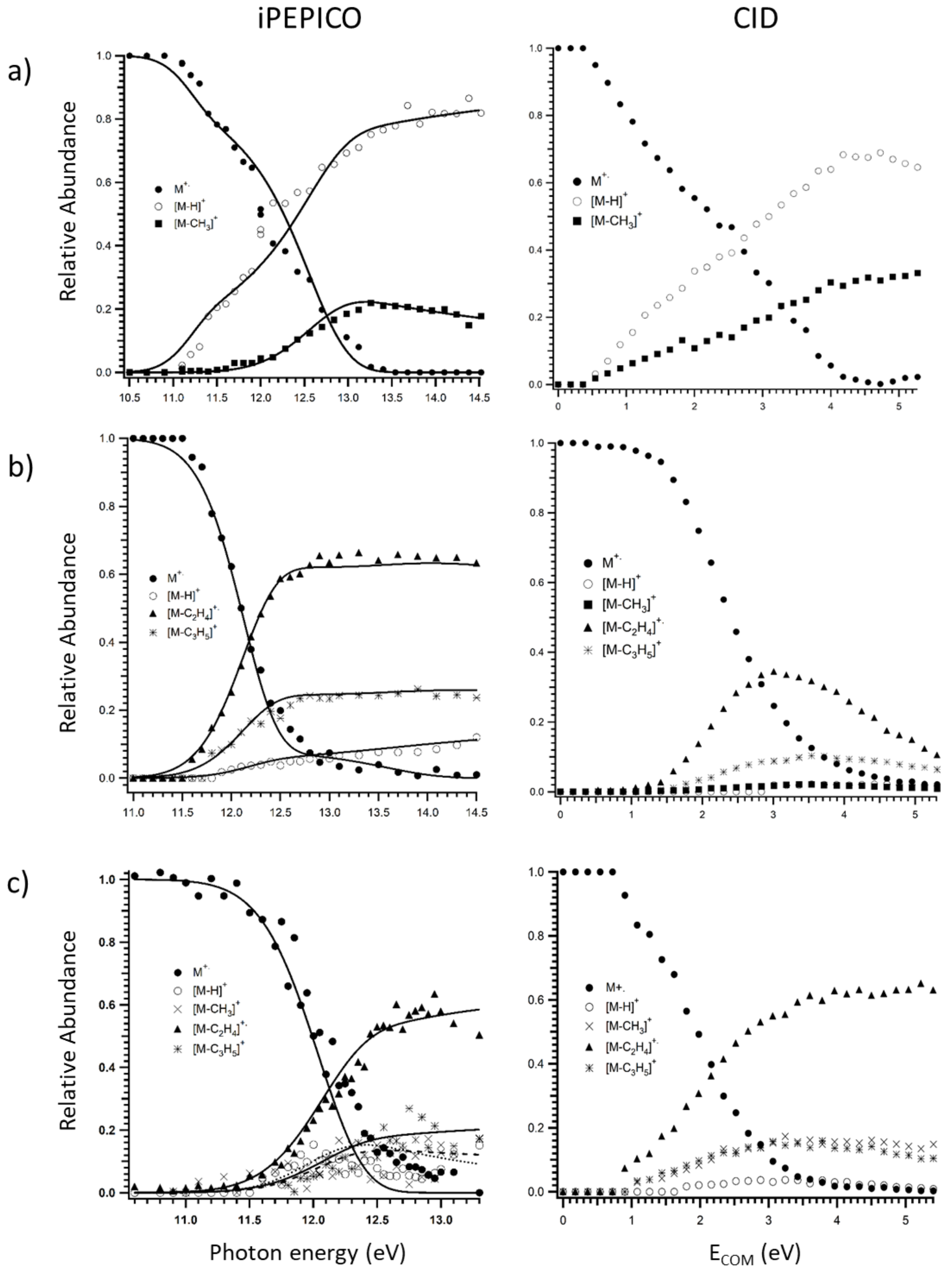

Figure 21. iPEPICO and CID breakdown curves for a) DHA+•, b) OHA+• and c) THP+•. Lines are the RRKM fit to the experimental iPEPICO data.

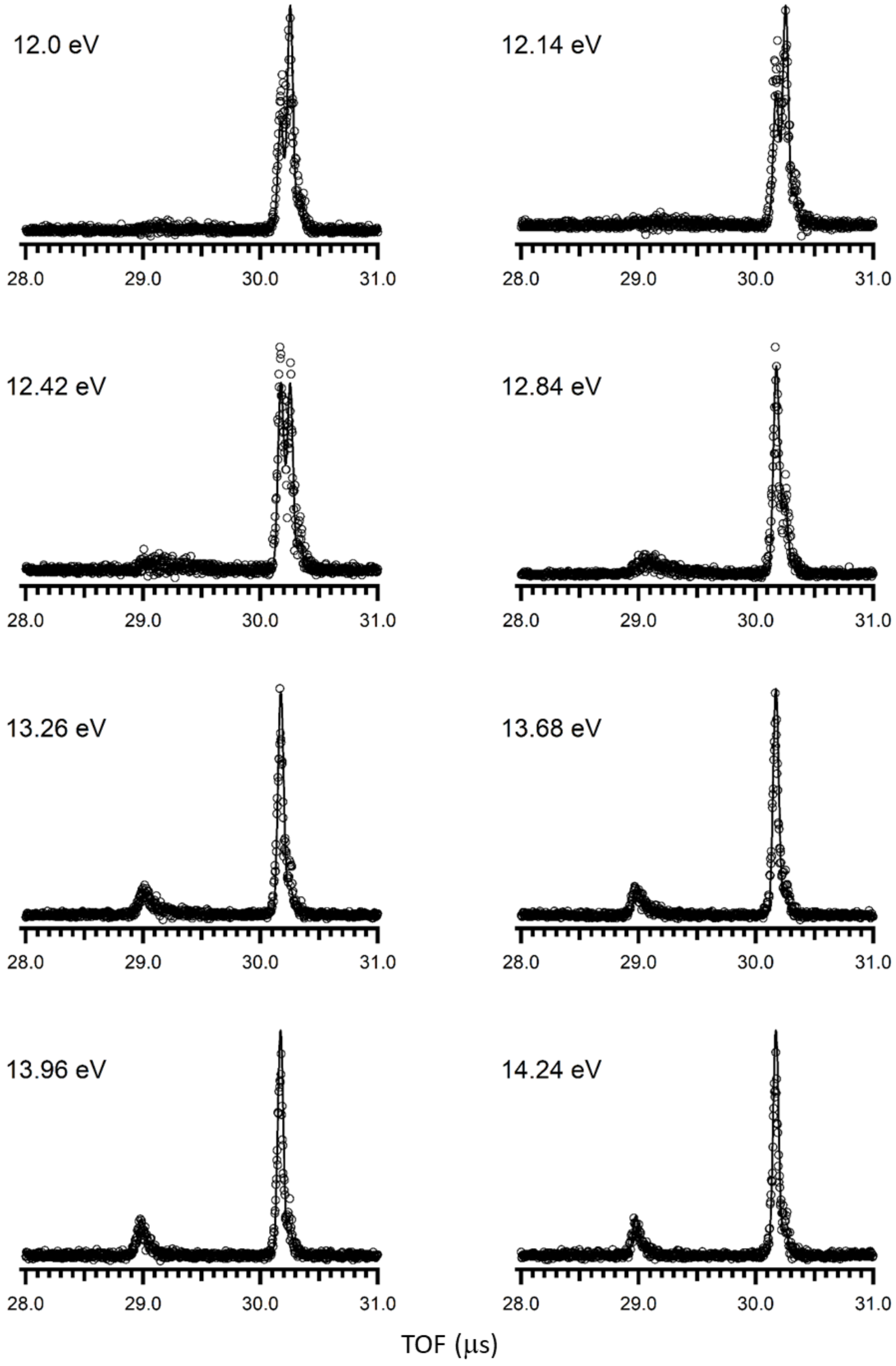

Figure 22. Representative TOF distributions for DHA+•. Solid lines are the RRKM fit to the experimental data.

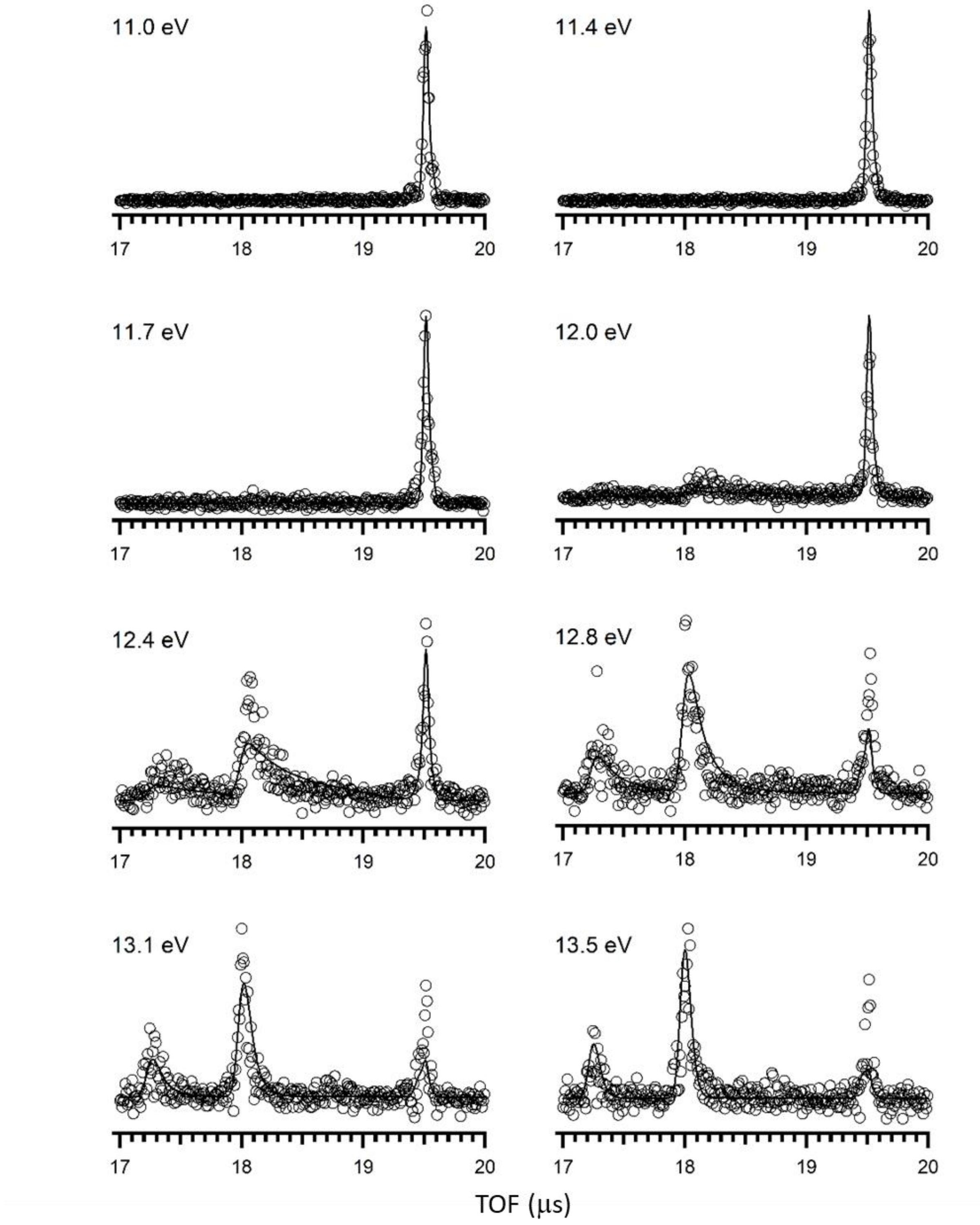

Figure 23. Representative TOF distributions for OHA+•. Solid lines are the RRKM fit to the experimental data.

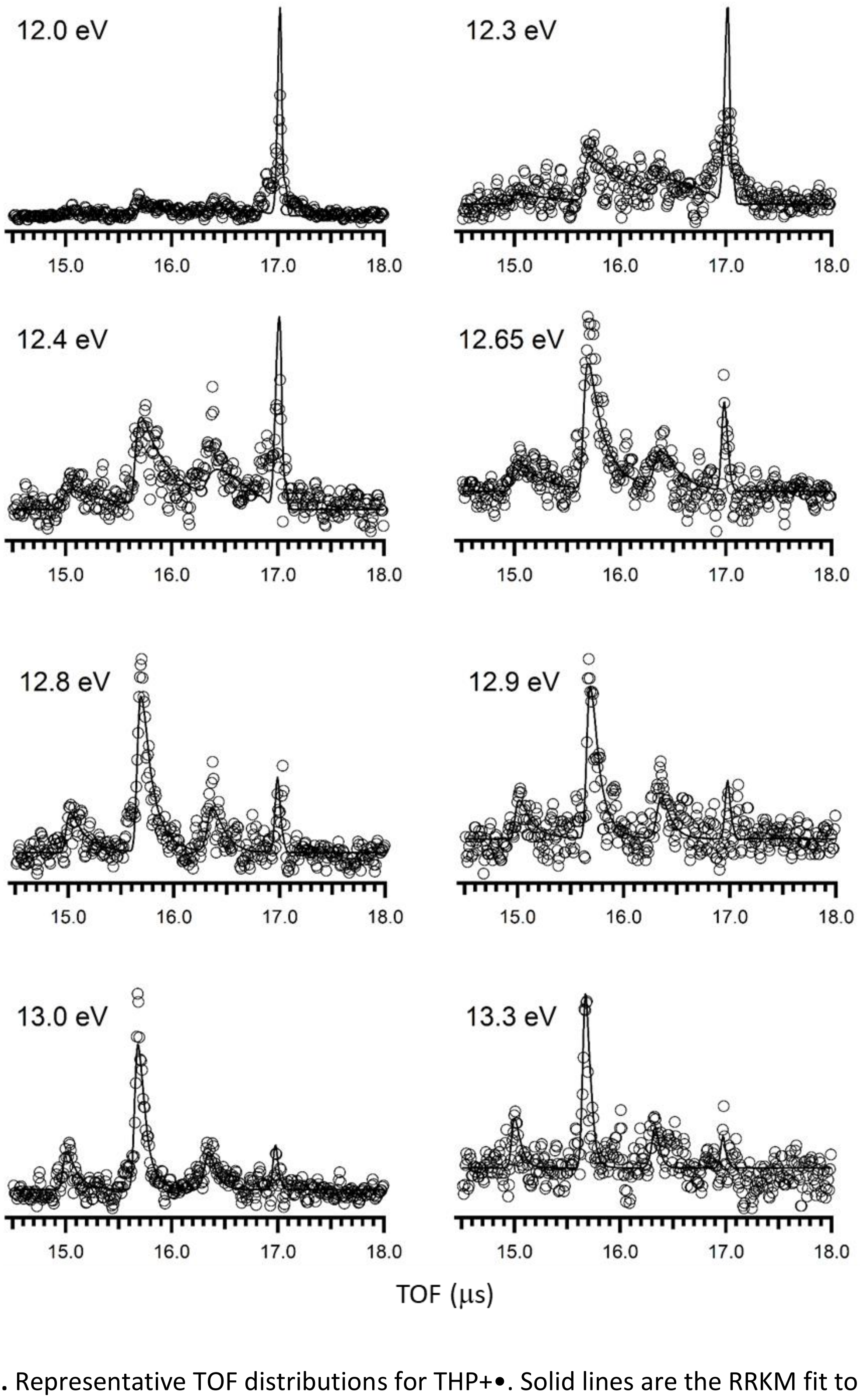

Figure 24. Representative TOF distributions for THP+•. Solid lines are the RRKM fit to the experimental data.

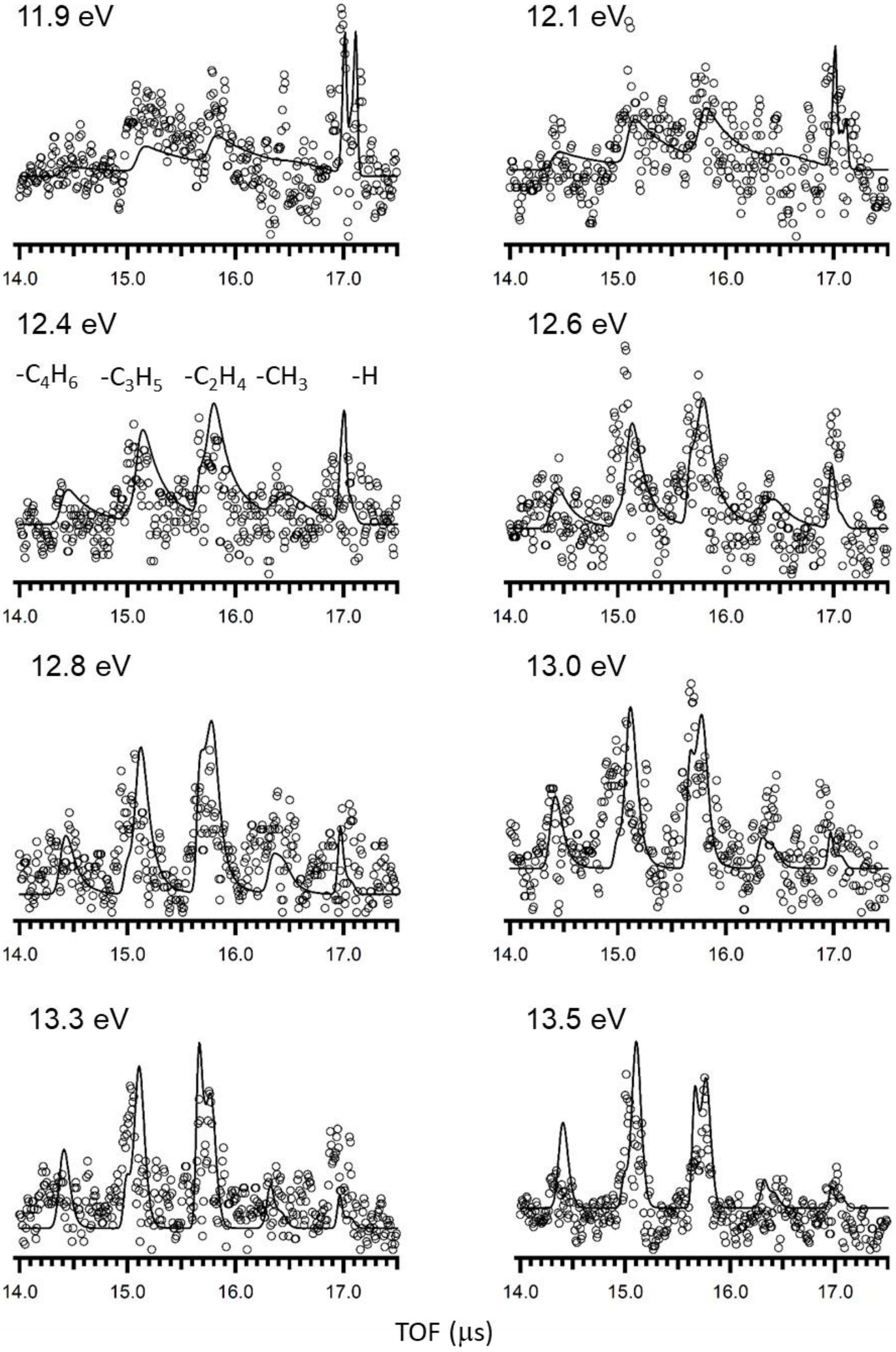

Figure 25. Representative TOF distributions for HHP+•. Solid lines are the RRKM fit to the experimental data, with the respective fits for THP+• added.

4.2.1. RRKM Modeling Results.

RRKM modeling of the experimental breakdown curves and time-of-flight distributions yielded the energetic results summarized in Table 2. By analogy to previous work on $DHN^{+\bullet}$ and $DHP^{+\bullet}$ [33], $DHA^{+\bullet}$ was modeled with a two-well potential surface with $H^{\bullet}$-loss originating from both the molecular ion and the isomer, while $CH_3^{\bullet}$-loss arose only from the isomer. The resulting 0 K reaction energies, relative to ionized $DHA^{+\bullet}$, were 1.93 eV for $H^{\bullet}$-loss from $DHA^{+\bullet}$, 1.91 eV from the isomer and 2.01 eV for $CH_3^{\bullet}$-loss from the isomer. The predicted barrier was 1.77 eV between $DHA^{+\bullet}$ and the isomer. $THP^{+\bullet}$ required a two-well mechanism previously used for tetralin. Here $H^{\bullet}$- and $CH_3^{\bullet}$-loss are relatively less abundant than they were in the case of tetralin, suggesting less isomerization to a methyl-substituted isomer prior to $CH_3^{\bullet}$-loss. $HHP^{+\bullet}$ exhibited all four reactions, plus an extra loss of C_4H_6 (RRKM derived reaction energy of 1.90 ± 0.02 eV) at higher energies; the derived energies are listed in Table 2. The same kinetic scheme was used as employed for $THP^{+\bullet}$, but with the extra channel (C_4H_6-loss) coming from the molecular ion. Due to the uncertainty inherent in the convolution process used for modeling the TOF distributions, we do not assign error limits to the $HHP^{+\bullet}$ data, and they should be taken as semi-quantitative. Modeling of the $OHA^{+\bullet}$ data yielded reaction energies of 2.13 ($H^{\bullet-}$loss), 2.03 (C_2H_4-loss) and 1.99 eV ($C_3H_5^{\bullet}$-loss). As with the other compounds, the data needed to be modeled with a two-well potential surface, but with all of the fragments coming from the molecular ion. The second well was needed to accurately predict the molecular ion abundance at high energy.

Table 3. RRKM-derived Energies (eV) for Neutral Loss Reactions in Hydrogenated PAH Ions, Relative to the Respective Molecular Ions.

Ion	H$^{\bullet}$	CH$_3^{\bullet}$	C$_2$H$_4$	C$_3$H$_5^{\bullet}$	TS	Isomer[a]	Ref
DHN$^{+\bullet}$	2.44 ± 0.1	2.57 ± 0.12*			1.75 ± 0.25	0.0	[33]
	2.22 ± 0.05*						
DHP$^{+\bullet}$	2.37 ± 0.12	2.38 ± 0.15					[33]
DHA$^{+\bullet}$	1.93 ± 0.07	1.75 ± 0.07*			1.7 ± 0.1	-0.26	
	1.65 ± 0.07*						
Tetralin$^{+\bullet}$	2.37 ± 0.02	1.72 ± 0.02	1.72 ± 0.02	2.31 ± 0.02	2.24 ± 0.02	-0.29	[71]
		1.66 ± 0.02*	1.53 ± 0.02*				
THP$^{+\bullet}$	1.19 ± 0.06 *	1.30 ± 0.06 *	2.17 ± 0.02	2.14 ± 0.02	1.77 ± 0.02	-0.29	
HHP$^{+\bullet}$	1.55*	1.53*	1.85	1.83	1.77[b]	-0.29[b]	
OHA$^{+\bullet}$	2.13 ± 0.05		2.03 ± 0.05	1.99 ± 0.05	1.99	-0.25	
c-Hexane$^{+\bullet}$	1.44	1.19	1.20	1.61			[81][c]

* Indicates the reaction was modeled originating from the isomer separated from the molecular ion by TS.

[a] Due to the large uncertainty in this value, error limits have not been assigned.

[b] Assumed to be the same value as in THP.

[c] Photoionization appearance energy values after subtraction of the IE.

The three dihydro-PAHs exhibit consistency in reaction energies and key isomerization barrier energy, Table 2. DHA$^{+\bullet}$ appears to have slightly lower reaction energies than the other two, perhaps due to H$^{\bullet}$-loss allowing electron delocalization across all three rings. The reaction energies for the four polyhydrogenated PAHs are fairly similar considering the more qualitative nature of the values for HHP$^{+\bullet}$. There is more variability in the energies for reactions originating from the isomer in the two-well surface employed to model the data. None of the hydrogenated PAHs have reaction energies comparable to those of ionized cyclohexane, which also dissociates by loss of ethyl radicals and propene [81]. It should be noted that the values for cyclohexane ions come from photoionization appearance energy measurements and deserve to be revisited. As ring size increases to decahydronapthalene, the electron ionization mass spectrum also exhibits loss of propyl and butyl radicals and butane neutrals [82], indicating that even octahydroanthracene does not quite behave as a saturated hydrocarbon.

4.2.2. Dissociation Reactions

The pathways for H$^\bullet$ and $CH_3{}^\bullet$-loss from DHA$^{+\bullet}$ were calculated at the B3-LYP/6-31+G(d,p) level of theory and are shown in Figure 26.

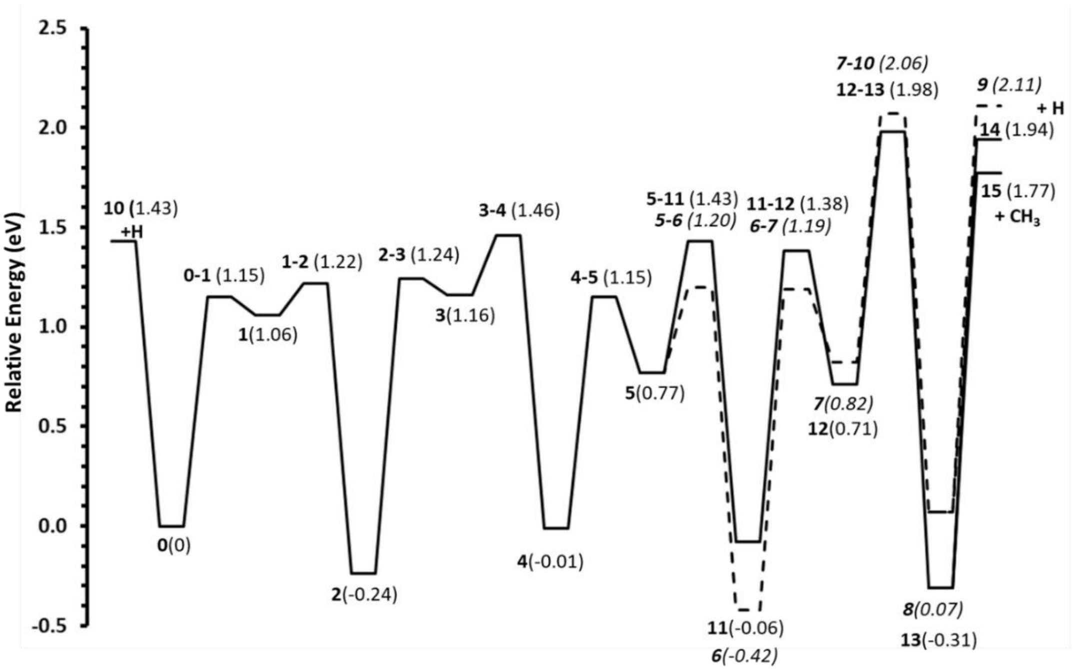

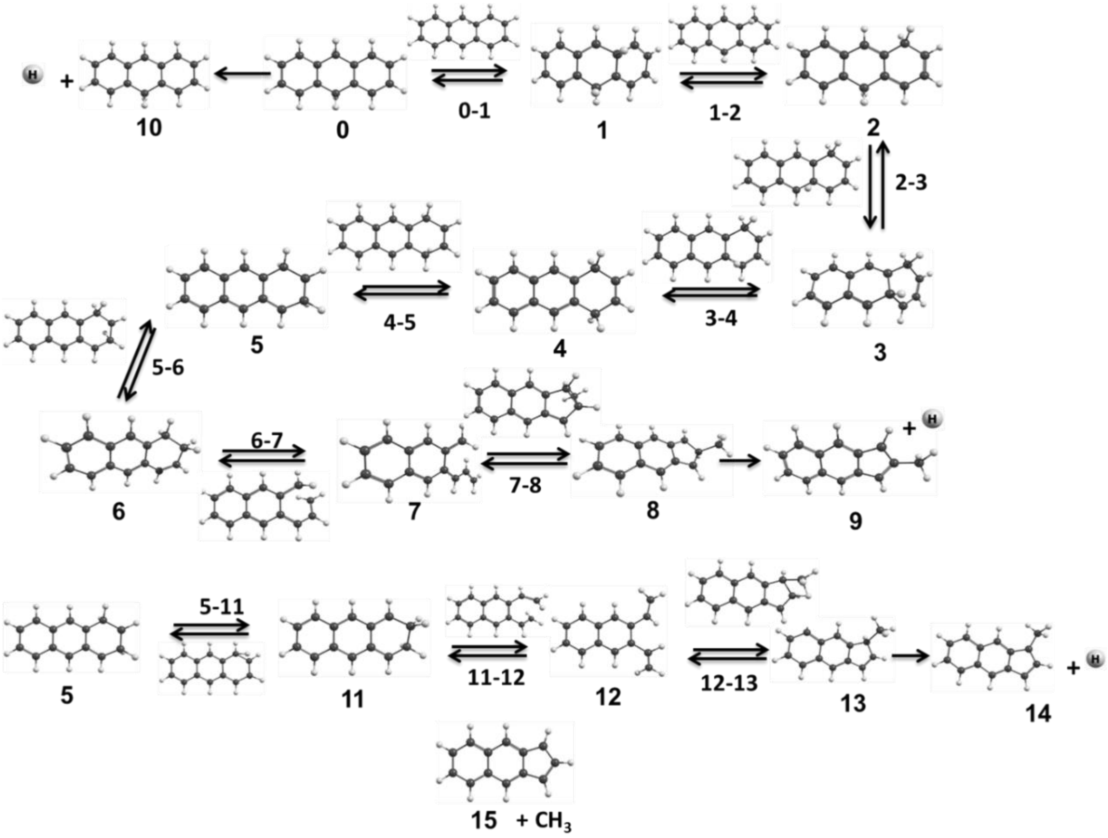

Figure 26. Calculated reaction pathways for H• atom and CH3•-loss from ionized DHA+• (B3-LYP/6-31G+(d,p) level of theory). Values in italics correspond to the dashed surface.

Isomerization occurs via a series of H-shift reactions forming 1,2-dihydroanthracene, **6**. This ion ring opens to **7**, followed by a concerted ring-closing/H-shift to form **8**. An alternative route can make the isomeric 2,3-dihydroanthracene, **11**, which leads to **13**. The energy requirement for the latter path is slightly lower. H$^{\bullet}$-loss can occur from one of the sp^3 carbons in the molecular ion or from either **8** or **11**, suggesting there should be two sources for [M-H]$^+$ in mass spectra, one from the molecular ion and one from the methylindene analogue, consistent with the kinetic model used to fit the experimental data. CH$_3^{\bullet}$-loss easily occurs from either **8** or **11** to form the same product ion, **15**. Simple H$^•$-loss from an sp^3 carbon in DHA$^{+•}$ costs only 1.43 eV but this is likely grossly underestimated at this level of theory, as was seen for tetralin.[71]

Pathways for the loss of C_2H_4 and $C_3H_5^•$ from OHA$^{+•}$ are presented in Figures 27 and 28. Both are analogous to those found for tetralin. C_2H_4 loss is mediated by H-transfer reactions leading to **18**, which can then ring-open and loss C_2H_4 to make an ethenylbenzene analogue, **20**. Figure 9. $C_3H_5^•$-loss also involves H-shift reactions leading to **21** which then ring-opens to **22**. A subsequent H-transfer lead to **23** which can then lose the allyl radical to make benzylium analogue **24**, Figure 10. The similarly between the dihydroPAH ions and between OHA$^{+•}$ and tetralin$^{+•}$ leads to the speculation that these mechanisms are conserved as a function of PAH size, as was observed for C_2H_2 loss from unsubstituted PAHs.[70]

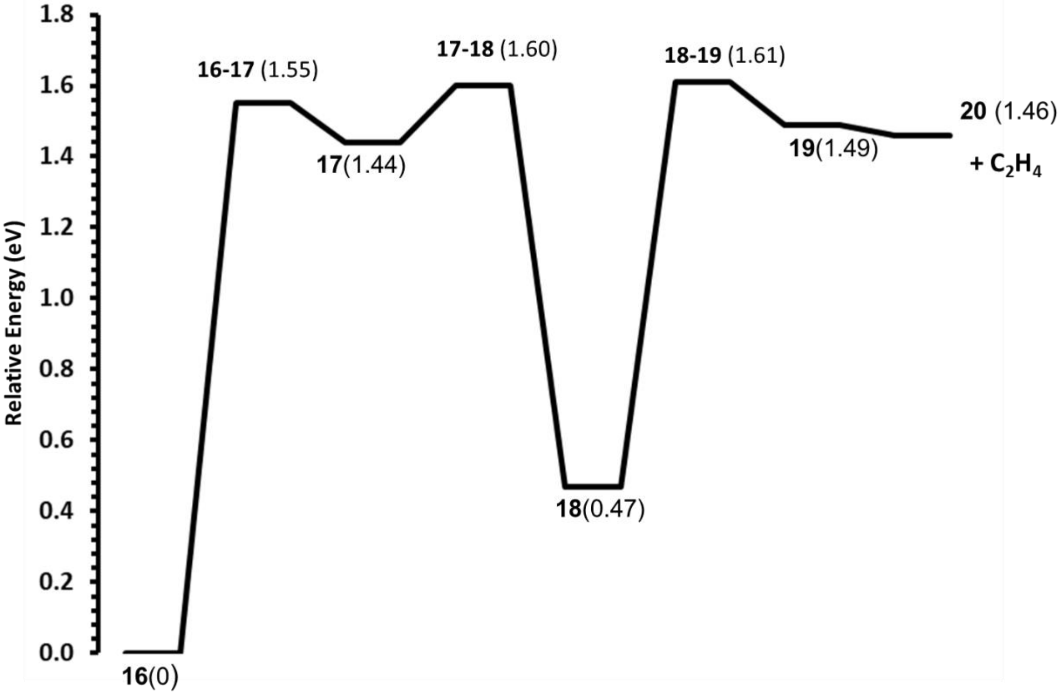

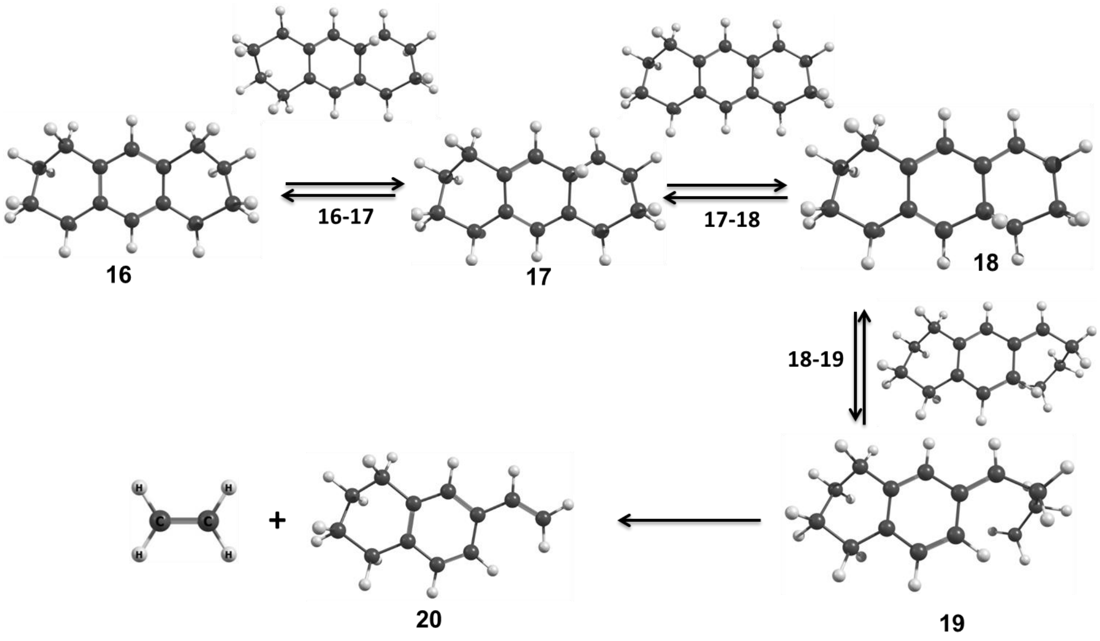

Figure 27. Calculated reaction pathway forming C2H4 from ionized OHA+• (B3-LYP/6-31+G(d,p) level of theory). Structure 19 is bound with respect to products on the electronic surface, but unbound when zero-point vibrational energy is added.

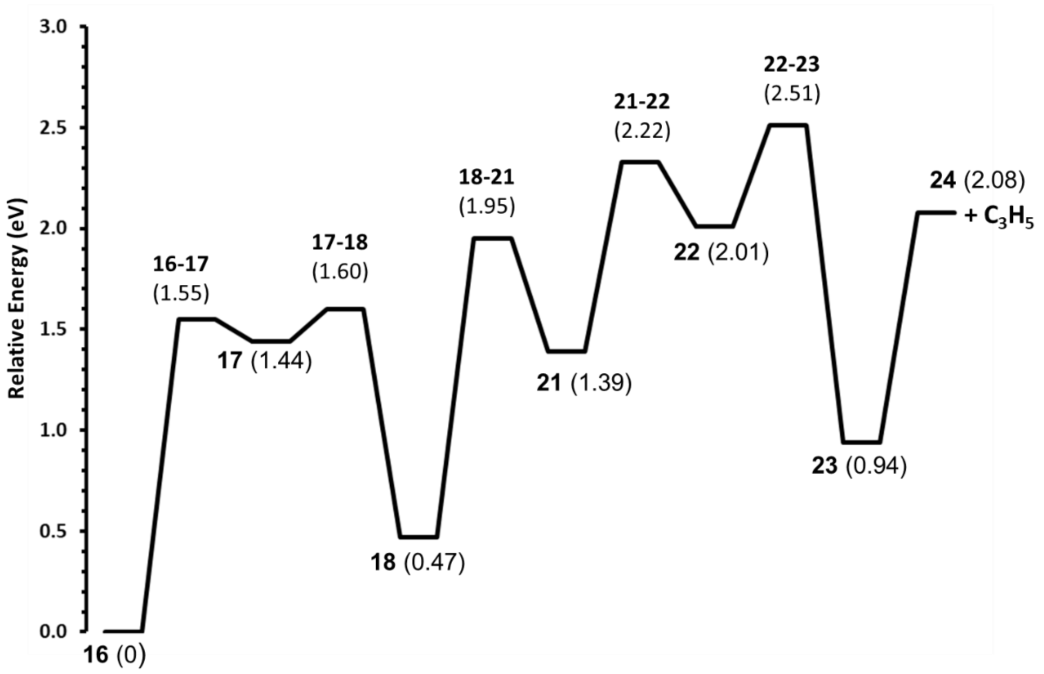

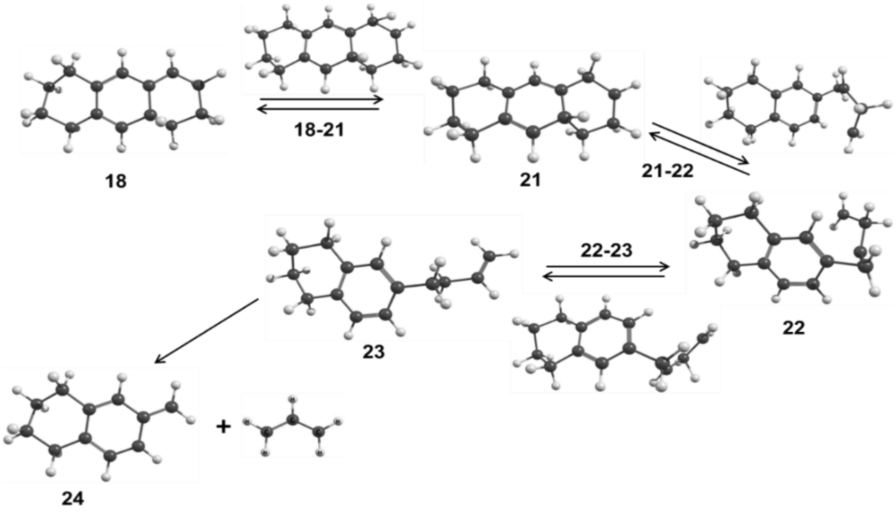

Figure 28. Calculated reaction pathway forming C3H5• from ionized OHA+• (B3-LYP/6-31G(d,p) level of theory).

It is difficult to relate the RRKM results to the energetics of a complex reaction pathway when there is no clear rate limiting transition state or single stable isomer. In the case of DHA$^{+\bullet}$, the predicted barrier of 1.7 eV is not out of line with the final calculated transition states **7-10** or **12-13**. The RRKM estimate of the isomer's relative energy, -0.26 eV, fits structures **6** and **13** while the calculated dissociation thresholds are in reasonable (but not fantastic) agreement with the RRKM estimates, given the uncertainty in the latter and the relatively low level of theory employed. In other words, the general shape of the reaction pathways is consistent between theory and the RRKM estimate. Modeling of the OHA$^{+\bullet}$ data yielded the reaction energies of 2.03 (C_2H_4-loss) and 1.99 eV ($C_3H_5^\bullet$-loss). The former is higher than the energetics in Figure 9. The energy for $C_3H_5^\bullet$-loss agrees with the calculated product energies in Figure 28, but is low considering the high energy transition states involved in the illustrated pathway (notably **21-22** and **22-23**), suggesting there could be an alternative to the presented path.

Chapter 4: Conclusion

Ion dissociation dynamics of 1,2,3,4-tetrahydronaphthalene (Tetralin) as a test case for hydrogenated PAHs and the impact on unimolecular chemistry of PAH radical cations (DHA and OHA) with the successive hydrogen addition has been studied using iPEPICO, atmospheric pressure chemical ionization (APCI) – collision induced dissociation (CID) mass spectrometry and Gaussian calculation.

Ionized tetralin, the simplest poly-hydrogenated PAH, exhibits unimolecular reactions reminiscent to those of ionized 1,2-dihydronaphthalene and cyclohexane, which has been shown also to dissociate by loss of $H^•$, $CH_3^•$, C_2H_4 and $C_3H_5^•$ under electron- and photo-ionization.[66] The molecular ion can undergo isomerization by H-atom transfer and ring-opening reactions to yield $H^•$, $CH_3^•$, C_2H_4 and $C_3H_5^•$ neutral products, the latter producing the benzyl cation rather than the lower energy tropylium ion. In addition, the molecular ion isomerizes to the 1-methylindane ion structure over a barrier of 2.24 eV (RRKM modeling) which then can go on to produce $CH_3^•$ and C_2H_4. Isomerization is dominated by facile H-atom migration to the unsaturated ring carbons.

The dissociation of di-, tetra-, hexa- and octa-hydrogenated anthracene and phenanthrene ions reveals two general conclusions. The trend in reactivity in going from $DHA^{+•}$ to $THP^{+•}$, $HHP^{+•}$ and ultimately $OHA^{+•}$ sees decreasing abundance of $H^•$ and $CH_3^•$-loss and an increasing dominance of the formation of C_2H_4, $C_3H_5^•$ and higher hydrocarbons with degree of hydrogenation as isomerization to a methyl-substituted ion becomes less significant. As this isomerization decreases in significance, the ions become sources of small hydrocarbon molecules and not hydrogen atoms or molecules. There also appears to be conservation of the dissociation mechanisms for structurally-related PAH ions, as was previously seen for C_2H_2 loss from unsubstituted PAHs [70]. This suggests that PAHs act as sponges, soaking up hydrogen, and are not a source of H_2 in the ISM.

Based on these results obtained from this study of the ion chemistry of ionized PAH molecules, we can see that all the techniques used play roles that complement each other.

References

(1) Nuth III, A. J.; Charnley, B. S.; Johnson, M. N; Chemical Processes in the Interstellar Medium 147-161.

(2) Cronin, J. R.; Chang, S. Organic Matter in Meteorites: Molecular and Isotopic Analyses of the Murchison Meteorite, *NATO Advanced Study Institute and 2. International School of Space Chemistry: The chemistry of life's origins* 1993, 209-258.

(3) Botta, O.; Glavin, P. D.; Kminek, G.; Bada, L. J.; Relative Amino Acid Concentrations as a Signature for Parent Body Processes of Carbonaceous Chondrites, *Kluwer Academic Publishers,* 2002, 143–163.

(4) Allamandola, L. J.; Interstellar Polycyclic Aromatic Hydrocarbons; *American Chemical Society*: United States, 1989.

(5) Puget, J. L.; Léger, A. A.; New Component of the Interstellar Matter: Small Grains and Large Aromatic Molecules *Annual Review of Astronomy and Astrophysics,* 1989, *27*, 161-198.

(6) Schlemper, E. O.; Thompson, R. C.; Fair, C. K.; Ross, F. K.; Appelman, E. H.; Basile, L. J.; Structure, Deformation Density and Atomic Charges in Potassium Hydrogenperoxomonosulfate Monohydrate, $KHSO_5.H_2O$ *Acta Crystallographica Section C* 1984, *40*, 1781-1785.

(7) Frenklach, M.; Feigelson, E. D.; Formation of Polycyclic Aromatic Hydrocarbons in Circumstellar Envelopes *The Astrophysical Journal,* 1989, *341*, 372.

(8) Bettens, R. P. A.; Herbst, E.; The Abundance of Very Large Hydrocarbons and Carbon Clusters in the Diffuse Interstellar Medium *The Astrophysical Journal,* 1996, *468*, 686.

(9) Ehrenfreund, P.; Bernstein, M. P.; Dworkin, J. P.; Sandford, S. A.; Allamandola, L. J. The Photostability of Amino Acids in Space, *The Astrophysical Journal,* 2001, *550*, L95-L99.

(10) Joblin, C.; Tielens, A. G. G. M., Eds.; *PAHs and the Universe: A Symposium to Celebrate the 25th Anniversary of the Pah Hypothesis*; EAS Publications Series, 2011; Vol. 46.

(11) Castellanos, P.; Candian, A.; Andrews, H.; Tielens, A. G. G. M.; Photoinduced Polycyclic Aromatic Hydrocarbon Dehydrogenation *A&A,* 2018, *616*, A167.

(12) Grein, F.; The ClO_4 Radical: A Theoretical Study on Ground and Excited States *Molecular Physics,* 2009, *107*, 2005-2013.

(13) Tielens, A. G. G. M.; Interstellar Polycyclic Aromatic Hydrocarbon Molecules *Annual Review of Astronomy and Astrophysics,* 2008, *46*, 289-337.

(14) Gillett, F. C.; Forrest, W.; Merrill, K. M.; 8-13 Micron Spectra of Ngc 7027, Bd +30 3639, and Ngc 6572 *Astrophys. J.,* 1973, *183*, 87-93.

(15) Willner, S. P.; Puetter, R. C.; Russell, R. W.; Soifer, B. T.; Unidentified Infrared Spectral Features *Astrophys Space Sci.,* 1979, *65*, 95-101.

(16) Gould, R. J.; Salpeter, E. E.; The Interstellar Abundance of the Hydrogen Molecule. I. Basic Processes *Astrophys J.,* 1963, *138*, 393-407.

(17) Cazaux, S.; Morisset, S.; Spaans, M.; Allouche, A.; When Sticking Influences H_2 Formation *A&A,* 2011, *535*, A27.

(18) Lemaire, J. L.; Vidali, G.; Baouche, S.; Chehrouri, M.; Chaabouni, H.; Mokrane, H.; Competing Mechanisms of Molecular Hydrogen Formation in Conditions Relevant to the Interstellar Medium *Astrophy. J.,* 2010, *725*, L156-L160.

(19) Thrower, J. D.; Jørgensen, B.; Friis, E. E.; Baouche, S.; Mennella, V.; Luntz, A. C.; Andersen, M.; Hammer, B.; Hornekær, L.; Experimental Evidence for the Formation of Highly

Superhydrogenated Polycyclic Aromatic Hydrocarbons through H Atom Addition and Their Catalytic Role in H_2 Formation *Astrophy. J.,* 2012, *752*, 3.

(20) Vala, M.; Szczepanski, J.; Oomens, J.; Steill, J. D.; H_2 Ejection from Polycyclic Aromatic Hydrocarbons: Infrared Multiphoton Dissociation Study of Protonated 1,2-Dihydronaphthalene *J. Am. Chem. Soc.,* 2009, *131*, 5784-5791.

(21) Rauls, E.; Hornekær, L.; Catalyzed Routes to Molecular Hydrogen Formation and Hydrogen Addition Reactions on Neutral Polycyclic Aromatic Hydrocarbons under Interstellar Conditions *Astrophy. J.,* 2008, *679*, 531-536.

(22) Bauschlicher, J. C. W.; The Reaction of Polycyclic Aromatic Hydrocarbon Cations with Hydrogen Atoms: The Astrophysical Implications *Astrophy. J.,* 1998, *509*, L125-L127.

(23) Hirama, M.; Tokosumi, T.; Ishida, T.; Aihara, J.-i.; Possible Molecular Hydrogen Formation Mediated by the Inner and Outer Carbon Atoms of Typical Pah Cations *Chem. Phys.,* 2004, *305*, 307-316.

(24) Cassam-Chenaï, P.; Pauzat, F.; Ellinger, Y.; Is Stripping of Polycyclic Aromatic Hydrocarbons a Route to Molecular Hydrogen? *AIP Conf. Proceed.,* 1994, *312*, 543-547.

(25) Kapinus, V. A.; Photophysical Properties of Protonated Aromatic Hydrocarbons, California Institute of Technology, 2005.

(26) Reitsma, G.; Boschman, L.; J. Deuzeman, M.; Gonzalez-Magana, O.; Hoekstra, S.; Cazaux, S.; Hoekstra, R.; Schlathölter, T.; Deexcitation Dynamics of Superhydrogenated Polycyclic Aromatic Hydrocarbon Cations after Soft-X-Ray Absorption *Phys. Rev. Lett.,* 2014, *113*, 053002.

(27) Wolf, M.; Kiefer, H. V.; Langeland, J.; Andersen, L. H.; Zettergren, H.; Schmidt, H. T.; Cederquist, H.; Stockett, M. H.; Photo-Stability of Super-Hydrogenated Pahs *Astrophy. J.,* 2016, *832*, 24.

(28) Wolf, M.; Giacomozzi, L.; Gatchell, M.; de Ruette, N.; Stockett, M. H.; Schmidt, H. T.; Cederquist, H.; Zettergren, H.; Hydrogenated Pyrene: Statistical Single-Carbon Loss Below the Knockout Threshold *Euro. Phys. J.,* 2016, *70*, 85.

(29) Gatchell, M.; Stockett, M. H.; de Ruette, N.; Chen, T.; Giacomozzi, L.; Nascimento, R. F.; Wolf, M.; Anderson, E. K.; Delaunay, R.; Vizcaino, V.; Failure of Hydrogenation in Protecting Polycyclic Aromatic Hydrocarbons from Fragmentation *Phys. Rev. A.,* 2015, *92*, 050702.

(30) Rapacioli, M.; Cazaux, S.; Foley, N.; Simon, A.; Hoekstra, R.; Schlathölter, T.; Atomic Hydrogen Interactions with Gas-Phase Coronene Cations: Hydrogenation Versus Fragmentation *Phys. Chem. Chem. Phys.,* 2018, *20*, 22427-22438.

(31) Cazaux, S.; Arribard, Y.; Egorov, D.; Palotás, J.; Hoekstra, R.; Berden, G.; Oomens, J.; Schlathölter, T.; The Sequence of Coronene Hydrogenation Revealed by Gas-Phase Ir Spectroscopy *Astrophy. J.,* 2019, *875*, 27.

(32) Cazaux, S.; Boschman, L.; Rougeau, N.; Reitsma, G.; Hoekstra, R.; Teillet-Billy, D.; Morisset, S.; Spaans, M.; Schlathölter, T.; The Sequence to Hydrogenate Coronene Cations: A Journey Guided by Magic Numbers *Sci. Rep.,* 2016, *6*, 19835.

(33) West, B.; Joblin, C.; Blanchet, V.; Bodi, A.; Sztáray, B.; Mayer, P. M.; Dynamics of Hydrogen and Methyl Radical Loss from Ionized Dihydro-Polycyclic Aromatic Hydrocarbons: A Tandem Mass Spectrometry and Imaging Photoelectron−Photoion Coincidence (iPEPICO) Study of Dihydronaphthalene and Dihydrophenanthrene *J. Phys. Chem. A.,* 2014, *118*, 1807−1816.

(34) Todd, P. J.; McLafferty, F. W.; Tandem Mass Spectrometry; *Wiley-Interscience*: New York, 1983.

(35) Carroll, D. I.; Dzidic, I.; Stillwell, R. N.; Haegele, K. D.; Horning, E. C.; Atmospheric Pressure Ionization Mass Spectrometry. Corona Discharge Ion Source for Use in a Liquid Chromatograph-Mass Spectrometer-Computer Analytical System *Analytical Chemistry,* 1975, *47*, 2369-2373.

(36) Busch, K. L.; Glish, G. L.; McLuckey, S. A.; Mass Spectrometry/Mass Spectrometry; *VCH Publishers*: New York, 1988.

(37) Sleno, L.; Volmer, D. A.; Ion Activation Methods for Tandem Mass Spectrometry *Journal of Mass Spectrometry,* 2004, *39*, 1091-1112.

(38) Bodi, A.; Sztaray, B.; Baer, T.; Johnson, M.; Gerber, T.; Data Acquisition Schemes for Continuous Two-Particle Time-of-Flight Coincidence Experiments *Rev. Sci. Instrum.,* 2007, *78*, 084102.

(39) Offerhaus, H. L.; Nicole, C.; Lépine, F.; Bordas, C.; Rosca-Pruna, F.; Vrakking, M. J. J.; A Magnifying Lens for Velocity Map Imaging of Electrons and Ions *Review of Scientific Instruments,* 2001, *72*, 3245-3248.

(40) Einstein, A.; Podolsky, B.; Rosen, N.; Can Quantum-Mechanical Description of Physical Reality Be Considered Complete? *Physical Review,* 1935, *47*, 777-780.

(41) Butler, K.; Jelfs, K.; Gren, W.; An Introduction to Computational Methods, 2008.

(42) Cramer, C. J.; *Essentials of Computational Chemistry: Theories and Models*; Wiley, 2005.

(43) Ghorpade, S. R.; Limaye, B. V.; A Geometric Approach to Saddle Points of Surfaces *Austral. Math. Soc. Gaz.,* 2009, *36*, 127-136.

(44) Lewars, E.; *Computational Chemistry: Introduction to the Theory and Applications of Molecular and Quantum Mechanics*; Springer, 2003.

(45) Krishnakumar, V.; Keresztury, G.; Sundius, T.; Ramasamy, R.; Simulation of Ir and Raman Spectra Based on Scaled Dft Force Fields: A Case Study of 2-(Methylthio) Benzonitrile, with Emphasis on Band Assignment *J. Mol. Struct.,* 2004, *702*, 9-21.

(46) Gargaud, M.; Amils, R.; Quintanilla, J. C.; Cleaves, H. J.; Irvine, W. M.; Pinti, D. L.; Viso, M.; Rice-Ramsperger-Kassel-Marcus, *Encyclopedia of Astrobiology*; Springer-Verlag Berlin Heidelberg, 2011; pp 1459-1459.

(47) Kim, G. S.; Nguyen, T. L.; Mebel, A. M.; Lin, S. H.; Nguyen, M. T.; Ab Initio/RRKM Study of the Potential Energy Surface of Triplet Ethylene and Product Branching Ratios of the C(3p) + CH_4 Reaction *J. Phys. Chem. A,* 2003, *107*, 1788-1796.

(48) Green, N.; *Comprehensive Chemical Kinetics: Unimolecular Kinetics, Part 1. The Reaction Step*; Elsevier Science, 2003.

(49) Baer, T.; Mayer, P. M.; Statistical Rice-Ramsperger-Kassel-Marcus Quaiequilibrium Theory Calculations in Mass Spectrometry *J. Am. Soc. Mass Spectrom.,* 1997, *8*, 103-115.

(50) Wang, H.; Gerken, W. J.; Wang, W.; Oehlschlaeger, M. A.; Experimental Study of the High-Temperature Autoignition of Tetralin *Energy & Fuels,* 2013, *27*, 5483-5487.

(51) Pitz, W. J.; Mueller, C. J.; Recent Progress in the Development of Diesel Surrogate Fuels *Prog. Energy Combust. Sci.,* 2011, *37*, 330-350.

(52) Tsang, W.; Cui, J. P.; Homogeneous Gas-Phase Decyclization of Tetralin and Benzocyclobutene *J. Am. Chem. Soc.,* 1990, *112*, 1665-1671.

(53) Li, C.; Suzuki, K.; Resources, Properties and Utilization of Tar *Resour. Conserv. Recycl.,* 2010, *54*, 905-915.

(54) Blum, P.; Sagner, A.; Tiehm, A.; Martus, P.; Wendel, T.; Grathwohl, P.; Importance of Heterocylic Aromatic Compounds in Monitored Natural Attenuation for Coal Tar Contaminated Aquifers: A Review *J. Contam. Hydrol.,* 2011, *126*, 181-194.

(55) Wang, Y.; Shah, N.; Huggins, F. E.; Huffman, G. P.; Hydrogen Production by Catalytic Dehydrogenation of Tetralin and Decalin over Stacked Cone Carbon Nanotube-Supported Pt Catalysts *Energy & Fuels,* 2006, *20*, 2612-2615.

(56) Vaikkinen, A.; Kauppila, T. J.; Kostiainen, R.; Charge Exchange Reaction in Dopant-Assisted Atmospheric Pressure Chemical Ionization and Atmospheric Pressure Photoionization *J. Am. Soc. Mass Spectrom.,* 2016, *27* 1291-1300.

(57) Sztáray, B.; Bodi, A.; Baer, T.; Modeling Unimolecular Reactions in Photoelectron Photoion Coincidence Experiments *J. Mass Spectrom.,* 2010, *45*, 1233-1245.

(58) Bodi, A.; Hemberger, P.; Gerber, T.; Sztáray, B.; A New Double Imaging Velocity Focusing Coincidence Experiment: iPEPICO. *Rev. Sci. Instrum.,* 2012, *83*, 083105.

(59) Hemberger, P.; Custodis, V. B. F.; Bodi, A.; Gerber, T.; Bokhoven, J. A. V.; Understanding the Mechanism of Catalytic Fast Pyrolysis by Unveiling Reactive Intermediates in Heterogeneous Catalysis *Nat. Commun.,* 2017, *8*, 15946.

(60) Sztáray, B.; Baer, T.; Suppression of Hot Electrons in Threshold Photoelectron Photoion Coincidence Spectroscopy Using Velocity Focusing Optics *Rev. Sci. Instr.,* 2003, *74*, 3763-3768.

(61) Frisch, M. J.; Trucks, G. W.; Schlegel, H. B.; Scuseria, G. E.; Robb, M. A.; Cheeseman, J. R.; Scalmani, G.; Barone, V.; Petersson, G. A.; Nakatsuji, H.; Gaussian 16 Rev. B.01 Wallingford, CT, 2016.

(62) Barone, V.; Bloino, J.; Biczysko, M.; Santoro, F.; Fully Integrated Approach to Compute Vibrationally Resolved Optical Spectra: From Small Molecules to Macrosystems *J. Chem. Theory Comput.,* 2009, *5*, 540-554.

(63) Baer, T.; Hase, W. L.; Unimolecular Reaction Dynamics*, Theory and Experiments*; *Oxford University Press*: New York, 1996.

(64) Baer, T.; Mayer, P. M.; Statistical RRKM/QET Calculations in Mass Spectrometry *J. Am. Soc. Mass Spectrom.,* 1997, *8*, 103-115.

(65) Beyer, T.; Swinehart, D. R.; Number of Multiply-Restricted Partitions [A1] (Algorithm 448) *ACM Commun.,* 1973, *16*, 379.

(66) Webbook, N. C.; *NIST Standard Reference Database Number 69*; National Institute of Standards and Technology: Gaithersburg, MD, 2005.

(67) Bouwman, J.; de Haas, A. J.; Oomens, J.; Spectroscopic Evidence for the Formation of Pentalene$^+$ in the Dissociative Ionization of Naphthalene *Chem. Commun.,* 2016, *52*, 2636-2638.

(68) West, B.; Rodriguez Castillo, S.; Sit, A.; Mohamad, S.; Lowe, B.; Joblin, C.; Bodi, A.; Mayer, P. M.; Unimolecular Reaction Energies for Polycyclic Aromatic Hydrocarbon Ions *Phys. Chem. Chem. Phys.,* 2018, *20*, 7195-7205.

(69) Solano, E. A.; Mayer, P. M.; A Complete Map of the Ion Chemistry of the Naphthalene Radical Cation? DFT and RRKM Modeling of a Complex Potential Energy Surface *J. Chem. Phys.,* 2015, *143*, 104305.

(70) West, B. J.; Lesniak, L.; Mayer, P. M.; Why Do Large PAHs Not Lose C_2H_2? *J. Phys. Chem A.,* 2019, *123*, 3569-3574.

(71) Diedhiou, M.; West, B. J.; Bouwman, J.; Mayer, P. M.; Ion Dissociation Dynamics of 1,2,3,4-Tetrahydronaphthalene: Tetralin as a Test Case for Hydrogenated PAHs *J. Phys. Chem. A.,* 2019, 123 (51), 10885-10892.

(72) Diedhiou, M.; Burner, J.; West, B. J.; Mayer, P. M.; Structure Affecting Energy in Polycyclic Aromatic Hydrocarbon Ions *Chem. Phys. Letters,* 2019, 726, 93-98.

(73) Burner, J.; West, B. J.; Mayer, P. M.; What Will Photo-Processing of Large, Ionized Amino-Substituted Polycyclic Aromatic Hydrocarbons Produce in the Interstellar Medium? *J. Phys. Chem. A.,* 2019, *123*, 5027-5034.

(74) West, B.; Lowe, B.; Mayer, P. M.; Unimolecular Dissociation of 1-Methylpyrene Cations: Why Are 1-Methylenepyrene Cations Formed and Not a Tropylium-Containing Ion? *J. Phys. Chem. A.,* 2018, *122*, 4730-4735.

(75) Burner, J.; West, B.; Mayer, P. M.; What Do We Expect from the Dissociation of Ionized Nitro-Substituted Polycyclic Aromatic Hydrocarbons in the Interstellar Medium? *Int J Mass Spectrom,* 2018, *434*, 81-86.

(76) West, B.; Sit, A.; Mohammad, S.; Bodi, A.; Hemberger, P.; Mayer, P. M.; Photodissociation of Polycyclic Aromatic Hydrocarbon Fragments: An iPEPICO Study of the TPES and Dissociation of Four Substituted Benzene Radical Cations *J. Phys. Chem. A.,* 2014, 11226-11234.

(77) West, B.; Sit, A.; Mohamed, S.; Joblin, C.; Blanchet, V.; Bodi, A.; Mayer, P. M.; Dissociation of the Anthracene Radical Cation: A Comparative Look at iPEPICO and Collision-Induced Dissociation Mass Spectrometry Results *J. Phys. Chem A.,* 2014, *118* 9870-9878.

(78) West, B.; Joblin, C.; Blanchet, V.; Bodi, A.; Sztáray, B.; Mayer, P. M.; On the Dissociation of the Naphthalene Radical Cation: New iPEPICO and Tandem Mass Spectrometry Results *J. Phys. Chem A.,* 2012, *116*, 10999-11007.

(79) Mayer, P. M.; Blanchet, V.; Joblin, C.; Threshold Photoelectron Study of Naphthalene, Anthracene, Pyrene, 1,2-Dihydronaphthalene, and 9,10-Dihydroanthracene *J. Chem. Phys.,* 2011, *134*, 244312.

(80) Meot-Ner, M.; Ion Thermochemistry of Low-Volatility Compounds in the Gas Phase. Polycyclic Aromatics: Ionization Energies, Proton and Hydrogen Affinities. Extrapolations to Graphite *J. Phys. Chem.,* 1980, *84*, 2716-2723.

(81) Sergeev, Y. L.; Akopyan, M. E.; Vilesov, F. I.; Chizhov, Y. V.; Photoionization Processes in Gaseous Cyclohexane, and Chloro- and Bromocyclohexane *High Energy Chem.,* 1973, *7*, 369 (418 in original).

(82) Lias, S. G.; Levin, R. D.; Kafafi, S. A.; Ion Energetics Data; *National Institute of Standards and Technology*: Gaithersburg MD, 20899.